Advances in the theory of III–V nanowire growth dynamics

2013 J. Phys. D: Appl. Phys. 46 313001

(http://iopscience.iop.org/0022-3727/46/31/313001)

J. Phys. D: Appl. Phys. **46** (2013) 313001 (29pp) doi:10.1088/0022-3727/46/31/313001

TOPICAL REVIEW

Advances in the theory of III–V nanowire growth dynamics

Peter Krogstrup[1], Henrik I Jørgensen[2], Erik Johnson[1], Morten Hannibal Madsen[1], Claus B. Sørensen[1], Anna Fontcuberta i Morral[3], Martin Aagesen[2], Jesper Nygård[1] and Frank Glas[4]

[1] Center for Quantum Devices, Niels Bohr Institute, University of Copenhagen, 2100 Copenhagen, Denmark
[2] SunFlake A/S, Universitetsparken 5, 2100 Copenhagen, Denmark
[3] Laboratoire des Materiaux Semiconducteurs, Ecole Polytechnique Fédérale de Lausanne, 1015 Lausanne, Switzerland
[4] CNRS, Laboratoire de Photonique et de Nanostructures, Route de Nozay, 91460 Marcoussis, France

E-mail: krogstrup@nbi.dk

Received 24 April 2013, in final form 21 June 2013
Published 12 July 2013
Online at stacks.iop.org/JPhysD/46/313001

Abstract
Nanowire (NW) crystal growth via the vapour–liquid–solid mechanism is a complex dynamic process involving interactions between many atoms of various thermodynamic states. With increasing speed over the last few decades many works have reported on various aspects of the growth mechanisms, both experimentally and theoretically. We will here propose a general continuum formalism for growth kinetics based on thermodynamic parameters and transition state kinetics. We use the formalism together with key elements of recent research to present a more overall treatment of III–V NW growth, which can serve as a basis to model and understand the dynamical mechanisms in terms of the basic control parameters, temperature and pressures/beam fluxes. Self-catalysed GaAs NW growth on Si substrates by molecular beam epitaxy is used as a model system.

(Some figures may appear in colour only in the online journal)

List of symbols and abbreviations

ERS:	equilibrium reference state
i:	refers to the ith element
j:	refers to the jth interface (unless other stated)
T:	substrate temperature
$T_{\mathrm{b},i}$:	beam flux temperature
$f_{i(,\perp)}$:	beam flux in the direction of the beam ($\perp$ refers to the flux perpendicular to the given interface)
f_i^{ERS}:	pressure equivalent beam (PEB) flux of element i needed to attain ERS conditions in the absence of a vapour phase.
p_i:	vapour pressure
$\rho_{j,i}$:	density of adatoms
x_i:	atomic fraction in the liquid phase $\bar{c}_{p,i}^{ERS}$
$\bar{c}_{p,i}$:	general symbol for the normalized atomic fraction in phase p
G_p:	global Gibbs free energy of the p phase
g_p:	Gibbs free energy per atom in phase p
$\mu_{p,i}^{(\infty)}$:	chemical potential in state p (∞ refers to infinitely large phases)
$\delta\mu_{p-\mathrm{ERS},i}$:	chemical potential in phase p with respect to the ERS
$\Delta\mu_{pq,i} = \delta\mu_{p-\mathrm{ERS},i} - \delta\mu_{q-\mathrm{ERS},i}$:	change in free energy due to a p to q atomic state transition

$\Delta\varepsilon_s$:	the difference in bulk free energy between the crystal with stacking sequence s and the standard reference (ERS)
$\delta g^{TS}_{pq,i}$:	the activation free energy per p atom needed to reach to transition state between p and q
$\Gamma_{pq,i}$:	p to q state transition flux
$\Delta\Gamma_{pq,i}$:	the net flux of the p to q state transitions
$S_{b(v),i}$:	sticking coefficient of beam or vapour elements
A_{pq}:	area of the pq interface
$\lambda_{j,i}$:	the effective adatom diffusion length
$D_{j,i}$:	the effective diffusivity coefficient
$\tau_{j,i}$:	the mean lifetime in the adatom state
$\Xi_{pq,i}$:	rate constant of the p to q transition
$\bar{Z}'_{pq}$:	the effective coordination number of the p to q transition. (') includes activation entropy.
$N_{p,i}$:	number of atoms of element i in phase p
$n_p^{(*)}$:	total number of III–V pairs in a cluster (* refers to the solid critical nucleus)
h_{ML}:	monolayer height along the growth axis
γ_j:	the tension of the j'th interface
L_{TL}:	total length of the triple phase line
φ_j:	the wetting angle given by Young's equation
$\theta(\omega)$:	the angle between the lv and the sl interface at ω
ω:	the angle between the middle of the side facet and the nucleation site, as measured from the centre of the topfacet
$\eta(\omega)$:	parameter determining the cross sectional shape at the growth interface, see equation (18)
R_l:	radius of curvature for the liquid–vapour interface
$I_{h\,k\,l}$:	the difference in interface energy between the $h\,k\,l$ facet and 'off facet' energy
Ω_p:	the average atomic volume in phase p.
I_i, $I_{i,des}$, $I_{i,inc}$:	the liquid sorption current, the liquid desorption current, the incorporation current
Z:	the Zeldovich factor
σ:	the ratio between vs and ls interfacial energies
$w_{h\,k\,l}$:	parameter specifying the half-width half maximum of the cusp in the gamma function around the $(h\,k\,l)$ facet
$c_{h\,k\,l}$:	correction parameter at high $w_{h\,k\,l}$ values
ξ:	contact angle of the constant curvature construction, see figure 14(b)
θ:	the angle from the topfacet to a given orientation
θ_T:	truncation angle of a given facet defined as $\theta_T = 90 - \theta$
GR_{planar}:	corresponding planar growth rate
Δt:	time step in simulation

1. Introduction

Nanowire (NW) crystals are wire-like single crystal structures with diameters typically constrained to tens of nanometers and with lengths of micrometres. The finite lateral size gives rise to many new physical properties which are not seen in bulk materials. In particular, there has been an enormous interest in controlling and understanding the crystal growth of semiconductor NWs over the recent years, as this is key for the control of the opto-electronic properties and NW morphology [1–8]. The vapour–liquid–solid (VLS) mechanism was first proposed in 1964 by Wagner and Ellis [9] as an explanation for unidirectional Si crystal growth in the presence of a liquid Au droplet. They concluded on the basis of a set of observations that the liquid phase acts as a sorption centre for growth material arriving from the vapour phase, and that the NW formation takes place by precipitation of growth material from the droplet. Today the VLS method is the most common way of achieving NW formation, and NWs are now being grown using various growth methods and with a wide range of materials such as oxides, group IV, III–V and II–VI semiconductors and metals. Here we focus on III–V materials, however, the general theoretical approach can be extended to other types of materials and growth mechanisms. The most typical methods for III–V NW formation are metal organic vapour phase epitaxy (MOVPE) and molecular beam epitaxy (MBE). In all cases there is a supersaturated liquid droplet which initiates and maintains NW growth. Typically, the growth direction is [1 1 1]B in the case of the cubic zinc blende (ZB) structure (ABC–ABC, 3C stacking) and [0 0 0 1]B for hexagonal wurtzite (WZ) structure (AB–AB, 2H stacking), see figures 1 and 2. Higher order stacking sequences such as 4H (ABCB–ABCB) and others are possible but are occurring very rarely and only in small segments, see Johansson *et al* [10] for a detailed discussion on higher order polytypes.

In the 1970s, theoreticians proposed the first advanced growth models, where fundamental aspects of VLS growth, such as axial and radial growth rates, size effects, nucleation and diffusion phenomenon were discussed (see for example Givargizov and references therein [12]). Even though groups started more detailed analyses of III–V NW growth in the 1990s [13], the VLS models from the 1970s where not significantly refined until Dubrovskii *et al* [14–16] in 2004 and Johansson *et al* [17] in 2005 proposed detailed VLS growth models of III–V NWs. Similar mechanisms such as the vapour–solid–solid mechanism (VSS) were also discovered as a variation of VLS [18]. Since then, the understanding of the complex growth mechanisms and the experimental control of the crystal phases, morphology and many different kind of heterostructure growth has undergone a huge progress. Today it is well accepted that group III species is adsorbed at the NW sidefacets and substrate surfaces and effectively diffuse to the growth region as adatoms [19–21], while group V species such as As and P are contributing to the axial growth primarily via either direct impingement from the beam (MBE) or as secondary absorbed species [22–24]. Today it is a fact that the shape of the NWs, and hence their potential applicability, is strongly dependent on the shape and

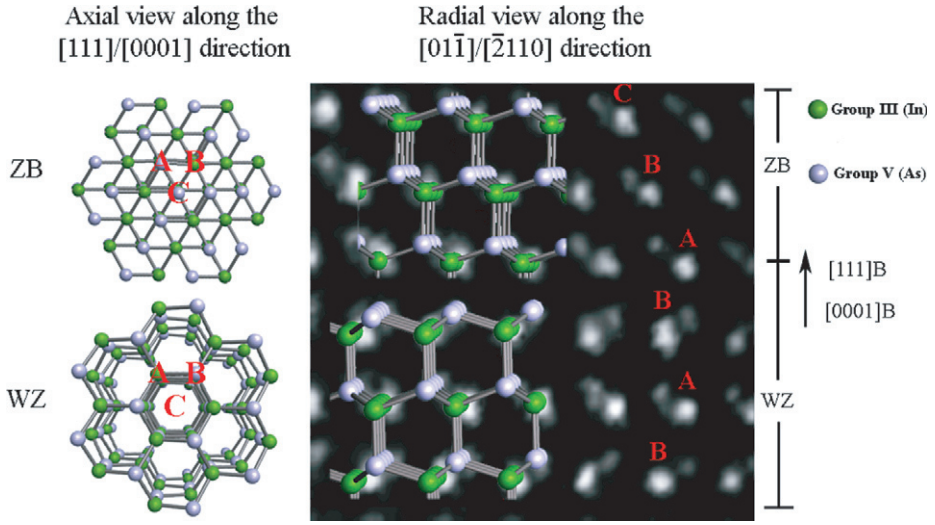

Figure 1. The two most common crystal structures in III–V NWs, ZB (ABC–ABC stacking) and WZ (AB–AB stacking), viewed along the axial [1 1 1]/[0 0 0 1] NW crystal growth directions and radial [0 1 −1]/[−2 1 1 0] crystal directions. The background of the high resolution radial view is a high angle annular dark field (HAADF) scanning transmission electron microscopy (STEM) image of a InAs NW, see [11].

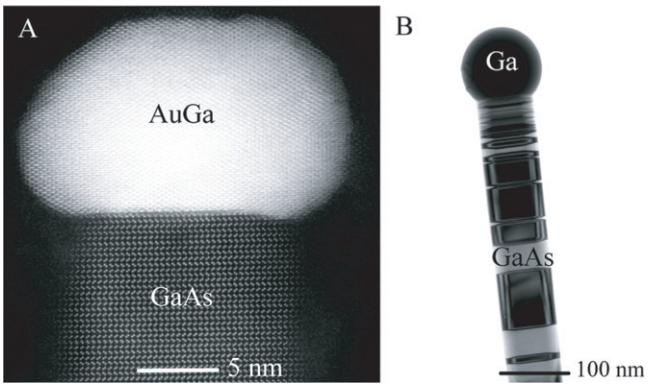

Figure 2. Two post-growth images of the most common types of growth of GaAs NWs via the VLS mechanisms; (*a*) Au catalysed and (*b*) self-catalysed growth. (*a*) shows a thin GaAs NW with a solidified AuGa crystal cap. The image was acquired with the high angle annular dark field (STEM) technique, using the probe corrected TEAM0.5 microscope. This technique makes it possible to resolve the atomic columns of the dumbbells revealing a perfect As-terminated WZ structure. In (*b*) a relatively thick multiply twinned ZB structured GaAs NW with a liquid Ga droplet on top, is shown. This image is acquired with a 200 keV CM20 microscope on film which is ideal for low magnification images with a large field of view. Both the AuGa and the Ga cap have been emptied of As upon cooling down to room temperature after growth termination.

morphology of the liquid–solid growth interface during growth [7, 25–29]. Thus, understanding and controlling the dynamics of NW growth is of great practical importance, and elucidating the effects of growth kinetics on especially the NW crystal shape, composition and on its crystalline quality have become major research topics [30–34]. Figure 2 shows post-growth transmission electron microscope (TEM) images of the two most common types of GaAs NW growth today, Au-catalysed and self-catalysed growth. Since the work of Wagner and Ellis [9], Au has always been the preferred material to promote axial NW growth via the VLS mechanism. However, since 2008 research on self-catalysed growth of GaAs NWs has received renewed interest [35, 36]. It is today a highly appreciated growth mode for GaAs NWs by MBE and the control of the morphology and crystal phases has quickly reached a high level (see for example the recent growth experiments by Yu *et al* [37] and Munchi *et al* [38]).

While most analyses of NW growth kinetics are based on post-growth characterization and static analyses of complete NWs, recent progress has been made experimentally by in-situ growth characterization [39–43] and *ex situ* study of NWs with markers inserted during growth [23, 44], and dynamic modelling [45–47]. For a more complete understanding of growth one should understand in detail the dependence of the basic control parameters (i.e. temperature and pressures/beam fluxes) on the growth mechanisms. Moreover, as local conditions on the growth front change during NW growth, it is necessary to include the time dependence in the analysis. However, to do this in a general manner, all essential features need to be incorporated into one coherent description of the growth dynamics, including a detailed treatment of all the main types of transitions involved in the process. Schwarz and Tersoff [45] presented in 2009 a pioneering continuum model for NW growth dynamics via the VLS process, where they could follow the evolution from a eutectic droplet at the substrate surface into a NW. Even though the kinetic equations governing this two-dimensional modelling is simplified to barrier-free kinetics without any explicit temperature dependence, it is able to describe some basic properties of the dynamical evolution. However, as will be explained here, transition barriers and temperature dependence play a very important role on the crystal structure and morphology. As an example, another pioneering work was presented two years earlier by Glas *et al* (2007) [25], who proposed that the liquid to solid phase transition at the (1 1 1) topfacet of III–V NWs was nucleation limited, and that the structure of each monolayer was determined by the structure of the two-dimensional nucleus which is needed to overcome the transition barrier. Thus, to understand the structural details

of the III–V NW growth, the temperature dependence cannot be neglected. In general, the temperature dependence on a given barrier limited transition rate is described with an Arrhenius dependence, or more specifically transition state theory [48]. Thus, here we will combine various theoretical predictions into more general dynamical and quantitative approach where the formalism, which will be explained in detail, is based on transition state kinetics driven by a Gibbs free energy minimization process. The modelling is based on the quantitative description of all the relevant dynamic processes, such as mass transfer, nucleation and dynamical reshaping of interfaces, and consists of many time-dependent and coupled equations involving the material parameters and growth conditions. We give various examples of modelling the self-catalysed GaAs NW growth in a MBE system and match the theoretical predictions directly with growth experiments, while stressing that the theoretical formalism also applies to other NW materials and growth systems. The aim of this review is to give a detailed theoretical insight into the III–V NW growth dynamics in an as pedagogical manner as possible. The focus will be on combining the knowledge which has been gained about III–V NW growth so far within the general framework of chemical kinetics, and to present a general and a novel theoretical formalism for III–V NW growth kinetics, which can serve as a tool to analyse and predict the evolution of NW growth, in terms of temperature and pressures/beam fluxes.

We will here give a brief outline of the content: section 2 presents the general theoretical formalism and is divided into three sections. Section 2.1 formulates the kinetics of the atomic movements, i.e. the probabilities of atomic state transitions in terms of rates, based on transition state theory. Here the effective transition rates between the various types of states are derived as a function of intrinsic parameters describing the 'local' environment. We then turn to the actual crystal formation at the liquid–solid interface in section 2.2. There, we discuss the framework needed to analyse the liquid–solid phase transition to a facetted NW crystal where transitions on certain facets can be nucleation limited. A specific topic which has attracted huge attention, is the mechanisms controlling the relative formation rates of ZB, WZ or other types of crystal structures in III–V NWs [25–28]. This is treated and discussed in detail in the framework of the present theory in sections 2.3 and 3.5. Section 3 show examples of self-catalysed GaAs NW growth experiments and how to use the theory to analyse and understand NW growth dynamics. First, growth simulations of the overall NW morphologies are presented in sections 3.1–3.4, and 3.5 present detailed simulations of the anisotropic liquid–solid NW growth dynamics and discuss the results.

2. Theoretical formalism

NW growth is a process far from thermodynamic equilibrium and in order to quantify the growth in terms of thermodynamic parameters, it is convenient to refer to an equilibrium reference state (ERS). Because the solid III/V stoichiometry is assumed to be fixed at 1 : 1 (which is verified to a very good accuracy), the chemical potential of the infinite solid phase is a function of temperature only and therefore serves as a natural reference state for the ERS. The ERS chemical potential of group III (or V) is equal to the liquid chemical potential when the liquid and solid are in equilibrium:

$$\mu^{\mathrm{ERS}}_{\mathrm{III(V)}} \equiv \mu^{\infty}_{\mathrm{l,III(V)}}(x^{\mathrm{ERS}}_{\mathrm{III}}, x^{\mathrm{ERS}}_{\mathrm{V}}) = \mu^{\infty}_{\mathrm{s,III}} + \mu^{\infty}_{\mathrm{s,V}} - \mu^{\infty}_{\mathrm{l,V(III)}}(x^{\mathrm{ERS}}_{\mathrm{III}}, x^{\mathrm{ERS}}_{\mathrm{V}}). \quad (1)$$

Here $x_i^{\mathrm{ERS}}(T)$ is the ERS mole fraction of group i in the liquid, and '∞' refers to large phases (i.e. without size effects, such as the Gibbs–Thomson effect). For the growth in a MBE chamber, we distinguish between five main types of states for each element i; beam flux (b, i), vapour (v, i), adatom/admolecule (a, i), liquid (l, i) and solid (s, i). Here the v states are all other states in the gas phase which are not a part of the direct beam flux, i.e. mainly what is reemitted from the neighbouring surfaces and evaporated form the droplets (and possibly reabsorbed). Six intrinsic parameters are needed to describe the ERS in the case of self-catalysed growth; temperature T, liquid concentration $x_{\mathrm{V}}^{\mathrm{ERS}}$ (group III concentration follows from $x_{\mathrm{III}} + x_{\mathrm{V}} = 1$), the partial vapour pressures $p_{\mathrm{III}}^{\mathrm{ERS}}$, $p_{\mathrm{V}}^{\mathrm{ERS}}$ and the ERS adatom densities $\rho_{\mathrm{III}}^{\mathrm{ERS}}$, $\rho_{\mathrm{V}}^{\mathrm{ERS}}$ (note that the beam flux cannot be a part of an equilibrium system). The ERS for self-catalysed growth has one degree of freedom, which means that the ERS is determined by the choice of one parameter, e.g. the temperature. For an example of calculating the ERS parameters for self-catalysed growth of GaAs or InAs we refer to section 3.1. For growth catalysed by a foreign element (such as gold) even if present only in the liquid phase, the system has one additional degree of freedom. This means that we can choose for instance both the temperature and the group III concentration to specify the state of the liquid. However, since the ERS is only a reference state it can be chosen as containing only two NW constituents, provided we know how to relate the thermodynamic quantities of the ternary liquid to those of the binary ERS. This is actually the case, since the chemical potentials of III–V liquids including Au have been calculated, see [49]. Thus, one can use the additional degree of freedom to choose the limit of no Au (i.e. $x_{\mathrm{III}}^{\mathrm{ERS}} = 1 - x_{\mathrm{V}}^{\mathrm{ERS}}$) and the ERS state can in fact be the same as for the self-catalysed system.

2.1. Growth kinetics

Within each of the main types of states (figure 3(*a*)), a 'local state' p is characterized by the mean intrinsic properties of some local surrounding (the 'local ensemble'), see figure 3(*b*), which is large enough to represent the thermodynamic characteristics and small enough to represent the local environment when the global system is out of equilibrium. At interfaces between two main types of states, a single interface is typically chosen, which means that one distinguish between particles on each side of the interface with local state properties depending only on the local environment of the main state to which they belong (figure 3(*c*)). A 'single Gibbs interface' is usually introduced to attach interface excess quantities to an assumed infinite sharp interface between two phases, i.e. no atoms belong to the interface, only excesses.

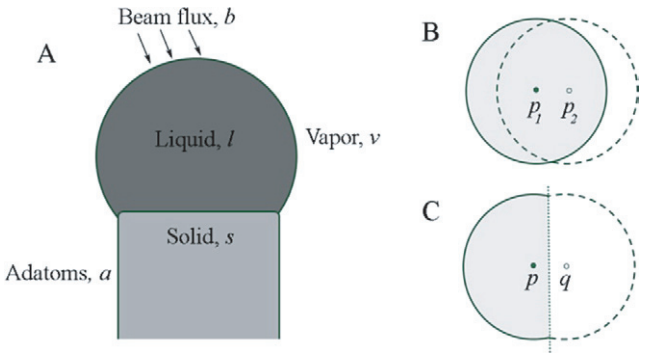

Figure 3. (*a*) The five types of states considered during the NW growth process. (*b*) The principle of describing atomic transition rates in a continuum language relies on the choice of small volume segments in the vicinity of the atomic state in which every property of the microstate p takes on average values of such ensemble. Within one of the main states shown in (*a*) two adjacent local states (here p_1 and p_2) are described with almost the same parameters. (*c*) Between two distinct types of states we choose a dividing interface where local states on each side of the phase boundary are described with mean parameters from a small volume segment within each respective main state. Thus in this formalism a discontinuous jump in the chemical potentials between two adjacent main states is possible during growth.

To describe the growth dynamics we need to treat the b and a states as separate states, but only consider interface excesses between the classical v, l and s phases. To insure a consistent treatment of the kinetics in terms of the intrinsic thermodynamic parameters, it is convenient to measure the chemical potentials of the all various states with respect to the chemical potential in the ERS,

$$\delta\mu_{p-\mathrm{ERS},i} = \mu_{p,i} - \mu_i^{\mathrm{ERS}}, \tag{2}$$

where $\mu_{p,i}$ are the chemical potential of the state p. The chemical potentials with respect to the four ERS states are

$$\delta\mu_{\mathrm{v}-\mathrm{ERS},i}(p_i, T) = k_{\mathrm{B}}T \ln\left(\frac{p_i}{p_i^{\mathrm{ERS}}}\right), \tag{3}$$

$$\delta\mu_{a_j-\mathrm{ERS,III(V)}}(\rho_{j,\mathrm{III}}, \rho_{j,\mathrm{V}}, T) = k_{\mathrm{B}}T \times \ln\left(\frac{\bar{\rho}_{j,\mathrm{III(V)}}(1-\bar{\rho}_{j,\mathrm{III}}^{\mathrm{ERS}}-\bar{\rho}_{j,\mathrm{V}}^{\mathrm{ERS}})}{\bar{\rho}_{j,\mathrm{III(V)}}^{\mathrm{ERS}}(1-\bar{\rho}_{j,\mathrm{III}}-\bar{\rho}_{j,\mathrm{V}})}\right), \tag{4}$$

$$\delta\mu_{\mathrm{l}-\mathrm{ERS},i}(x_{\mathrm{III}}, x_{\mathrm{V}}, T) = \mu_{\mathrm{l},i}^{\infty}(x_{\mathrm{III}}, x_{\mathrm{V}}, T) + \gamma_{\mathrm{vl}}\frac{\partial A_{\mathrm{vl}}}{\partial N_{\mathrm{l},i}} - \mu_i^{\mathrm{ERS}}, \tag{5}$$

$$\delta\mu_{\mathrm{s}-\mathrm{ERS,III-V}}^{X} = \sum_j \gamma_j \frac{\partial A_j}{\partial X}\frac{\partial X}{\partial N_{\mathrm{s,III-V}}} + \Delta\varepsilon_{\mathrm{s}}, \tag{6}$$

where $\rho_{j,i}$ is the adatom density on the jth facet and A_j and γ_j are the area and interface energy of the jth interface respectively. The form of equation (4) is a simplified version which stems from a detailed calculation of the partition function, see [50]. For the full expression, the following two terms should be added to equation (4): $-\bar{Z}_{j,\mathrm{aa}}(B_{j,\mathrm{III(V)}}(\bar{\rho}_{j,\mathrm{III(V)}} - \bar{\rho}_{j,\mathrm{III(V)}}^{\mathrm{ERS}}) + B_{j,\mathrm{III-V}}(\bar{\rho}_{j,\mathrm{V(III)}} - \bar{\rho}_{j,\mathrm{V(III)}}^{\mathrm{ERS}}))$. $\bar{Z}_{\mathrm{aa}}$ is a reaction constant (including coordination number) for facet j, and $B_{j,\mathrm{III(V)}}$ and $B_{j,\mathrm{III-V}}$ are the binding free energies for III–III(V–V) and III–V bonds on the j surface, respectively. If the adatom concentrations and binding energies are low, equation (4) can be approximated by an ideal behaviour, $\delta\mu_{a_j-\mathrm{ERS},i}(\rho_{j,i}, T) \cong k_{\mathrm{B}}T \ln(\rho_{j,i}/\rho_{j,i}^{\mathrm{ERS}})$, which strongly reduces computation time. The relative chemical potential of the solid $\delta\mu_{\mathrm{s}-\mathrm{ERS,III-V}}^{X}$ (equation (6)) in terms of a given parameter X, is the change in Gibbs free energy per pair due to a corresponding change in X, such as a length or an angle. In this continuum approach it describes the mean thermodynamic properties for the chosen parameter X. For a full description of the NW crystal an complete set of independent parameters, $\{X\}$, is needed. That is, adding matter to a nanosize crystal will change not only its volume, but also its shape, and therefore the interface excesses. In addition to its volume, the crystal must thus be defined by a set of parameters $\{X\}$ such as facet areas, projected facet heights, facet angles, edge lengths or local interface curvature. It is important to notice that $\{X\}$ is a chosen set of independent parameters that fully define the choice of crystal geometry (several choices are possible; an example is given in section 3.5). Then, the change of energy of the crystal when matter is added to it comprise a first term, associated to its change of shape, and a second term associated to its change of volume (which is simply related to the chemical potential of the reference infinite solid, as introduced in equation (1)). In the first term of equation (6), the independence of the X parameters and the effect of the changes of these parameters on the areas of the interfaces to which excess energies are associated, are taken into account. The second term is the difference in bulk cohesive energy between the standard reference of the ERS (typically ZB) and the actual formation structure s. The liquid–solid system will tend towards the equilibrium shape which is the one where the sum of all chemical potentials of the set are equal (See for example [51] for a treatment of a fully facetted solid in two dimensions using the concept of *weighted curvature* [52]). Note that if the crystal structure s is the same as the ERS, $\delta\mu_{\mathrm{s}-\mathrm{ERS,III-V}}^{X}$ is only a size effect as the bulk chemical potential is the same as the ERS (i.e. $\Delta\varepsilon_{\mathrm{s}} = 0$). See section 2.2 for more details. In addition to these interface size effects, it was suggested by Schmidt *et al* [53] and Schwartz and Tersoff [45] that an excess TL energy, which may arise from an in-balance of capillary forces at the TL, plays an important role on the dynamics of NW growth. See section A.6 in the appendix for a discussion.

As mentioned in the introduction, the general average rate at which a given $p \rightarrow q$ transition takes place depends exponentially on the Gibbs free energy of activation for reaching the transition state (TS), as $P_{pq,i} \propto \exp(-(\delta g_{pq,i}^{\mathrm{TS}}/k_{\mathrm{B}}T))$. $\delta g_{pq,i}^{\mathrm{TS}}$ is taken as the difference in free energy per atom between the state p (calculated from the thermodynamic parameters describing this state) and the transition state of the particle between p and q. If a given transition requires a bond-dissociation of molecules into single atoms (e.g. $\mathrm{As}_2 \rightarrow 2\mathrm{As}$), the dissociation enthalpy and entropy should be added to $\delta g_{pq,i}^{\mathrm{TS}}$.

The activation energy for reaching the *TS* can be written as $\delta g_{pq,i}^{\mathrm{TS}} = \delta g_{pq,i}^{\mathrm{TS,ERS}} - \delta\mu_{p-\mathrm{ERS},i}$, where $\delta g_{pq,i}^{\mathrm{TS,ERS}}$ is the activation

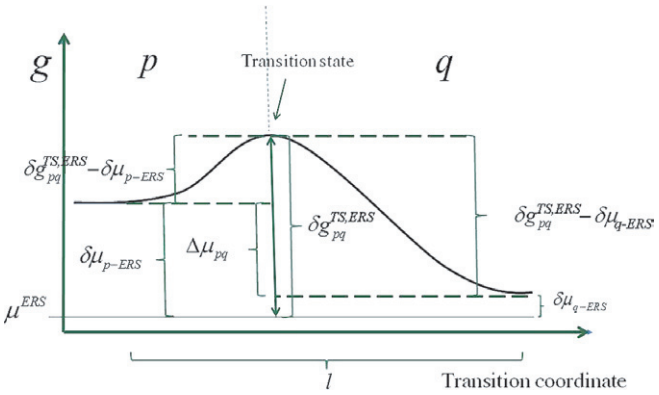

Figure 4. One-dimensional illustration of the free energy barrier associated with a pq state transition. Here the equilibrium transition state barrier is symmetric (i.e. $\delta g_{pq,i}^{\mathrm{TS,ERS}} = \delta g_{qp,i}^{\mathrm{TS,ERS}}$), as would be the case for a reversible state transition without requirements for dissociation/formation of bonds only one way. Note that even though the illustration is a typical sketch of a single particle barrier, it is treated in a continuum approach as the free energies are based on mean parameter values of the local ensemble.

energy for a p to q transition, and $\delta\mu_{p-\mathrm{ERS},i}$ is the chemical potential with respect to the ERS (see figure 4). The mean flux of atoms in the state p crossing the pq boundary per unit area (or length) is given by

$$\Gamma_{pq,i} = \begin{cases} \Xi_{pq,i}\bar{c}_{p,i}\exp\left(-\frac{\delta g_{pq,i}^{\mathrm{TS,ERS}} - \delta\mu_{p-\mathrm{ERS},i}}{k_{\mathrm{B}}T}\right) \\ \quad \text{if } \delta g_{pq,i}^{\mathrm{TS,ERS}} \geqslant \delta\mu_{p-\mathrm{ERS},i}, \\ \Xi_{pq,i}\bar{c}_{p,i} \\ \quad \text{if } \delta g_{pq,i}^{\mathrm{TS,ERS}} \leqslant \delta\mu_{p-\mathrm{ERS},i}, \end{cases} \tag{7}$$

where $\Xi_{pq,i}$ is a 'single atom flux' prefactor accounting for the number of attempts per atom to pass from the p state to the TS between p and q per unit time and unit area. $\bar{c}_{p,i}$ is the normalized density of group i atoms in state p, i.e. the probability of having an atom in the state. When $\delta g_{pq,i}^{\mathrm{TS,ERS}} < \delta\mu_{p-\mathrm{ERS},i}$, the transition is considered to be barrier-free. The form of $\Xi_{pq,i}$ can be very different depending on the type of transition. If the p state is part of a condensed state (a, l or s), the prefactor can be written as, $\Xi_{pq,i} = Z_{pq,i}\nu_{p,i}$, where $Z_{pq,i}$ is the steric factor[5] of the p to q transition per unit area and $\nu_{p,i}$ is a vibration frequency. For the gas states (b or v), we are only interested in the transitions to condensed states, and the prefactor can be written as, $\Xi_{\mathrm{b(v)},i} = S_{\mathrm{b(v)}q,i} f_{\mathrm{b(v)},i}^{\perp}/\bar{c}_{\mathrm{b(v)},i}$. Here $f_{\mathrm{b(v)},i}^{\perp}$ is the effective flux of atoms/molecules from the b (or v) states impinging normal to the interface of the $q = \mathrm{l}$ (or s) states. In order to calculate the effective flux across a pq boundary, the backward q to $p$flux needs to be subtracted from the forward p to q flux, $\Delta\Gamma_{pq,i} = \Gamma_{pq,i} - \Gamma_{qp,i}$. Under ERS conditions, we can apply an equation of *detailed balance* (i.e. the net fluxes of material across a boundary equal zero, $\Delta\Gamma_{pq,i}^{\mathrm{ERS}} = 0$), which implies that

$$\Xi_{qp,i} = \Xi_{pq,i}\frac{\bar{c}_{p,i}^{\mathrm{ERS}}}{\bar{c}_{q,i}^{\mathrm{ERS}}}\exp\left(-\frac{\Delta g_{pq,i}^{\mathrm{TS,ERS}}}{k_{\mathrm{B}}T}\right) \tag{8}$$

[5] The steric factor is here defined as the fraction of the total collision cross section of the p state which effectively has the transition state barrier specified for the $p \rightarrow q$ transition.

with $\Delta g_{pq,i}^{\mathrm{TS,ERS}} = \delta g_{pq,i}^{\mathrm{TS,ERS}} - \delta g_{qp,i}^{\mathrm{TS,ERS}}$ (Note that if the ERS transition state barrier is symmetric the exponential simply vanishes, as would be the case for a reversible state transition without requirements for dissociation/formation of bonds only one way). This is a general consequence of the detailed balance assumption when merging thermodynamics and transition state kinetics. The detailed balance provides an equilibrium relation between the ratios of coordination factors, attempt frequencies, possibly asymmetries for transition barriers at fixed ERS compositions. Finally, using equation (7) and equation (8), the net transition flux across the pq boundary is given as

$$\Delta\Gamma_{pq,i} = \Xi_{pq,i}\exp\left(-\frac{\delta g_{pq,i}^{\mathrm{TS,ERS}}}{k_{\mathrm{B}}T}\right)\left(\bar{c}_{p,i}\exp\left(\frac{\delta\mu_{p-\mathrm{ERS},i}}{k_{\mathrm{B}}T}\right) - \frac{\bar{c}_{p,i}^{\mathrm{ERS}}}{\bar{c}_{q,i}^{\mathrm{ERS}}}\bar{c}_{q,i}\exp\left(\frac{\delta\mu_{q-\mathrm{ERS},i}}{k_{\mathrm{B}}T}\right)\right). \tag{9}$$

As in equation (7), if $\delta g_{pq,i}^{\mathrm{T,ERS}} \leqslant \delta\mu_{p-\mathrm{ERS},i}$, i.e. $\exp(-((\delta g_{pq,i}^{\mathrm{TS,ERS}} - \delta\mu_{p-\mathrm{ERS},i})/k_{\mathrm{B}}T_p))$ is set to one. The entropy in the first exponential can be put into a new prefactor, $\Xi'_{pq,i} = \Xi_{pq,i}\exp(\Delta s_{pq,i}^{\mathrm{TS,ERS}}/k_{\mathrm{B}})$, that can be used as a temperature independent fitting parameter[6].

To keep track of the atomic movements involved in the axial NW growth, a mass transfer equation are used to describe the atomic flow to and from the liquid phase [22],

$$\frac{\mathrm{d}}{\mathrm{d}t}N_{\mathrm{l}} = I_{\mathrm{III}} + I_{\mathrm{V}} - I_{\mathrm{inc}}. \tag{10}$$

Here the liquid sorption currents I_i of group i atoms,

$$I_i = \int \Delta\Gamma_{\mathrm{al},i}\,\mathrm{d}l_{\mathrm{TL}} + \int \Delta\Gamma_{\mathrm{(vb)l},i}\,\mathrm{d}A_{\mathrm{vl}} \tag{11}$$

describe the effective 'adatom to liquid' and 'gas to liquid' currents. I_{inc} is the effective atomic incorporation current from the liquid into the solid, N_{l} is the number of atoms in the liquid, l_{TL} is the triple line (TL) length and A_{vl} is the projected liquid–vapour surface area [54]. If the equilibrium vapour pressure, p_i^{eq}, of a large liquid phase with a given composition is known (see section 3.1), the liquid to vapour transition rate from a liquid in such a state must fulfil the criteria, $\Gamma_{\mathrm{lv}} \leqslant p_i^{\mathrm{eq}}/\sqrt{2\pi m_i k_{\mathrm{B}}T}$, simply due to mass conservation. However, this criteria may be violated when size effects play an important role. Following the transition state approach, a simple version (sufficient in most cases) would be to assume no transition state barrier for sorption and a single vapour species for each element:

$$\Delta\Gamma_{\mathrm{(vb)l},i} \cong f_{i,\perp} - \frac{x_i}{x_i^{\mathrm{ERS}}}\frac{p_i^{\mathrm{ERS}}}{\sqrt{2\pi m_i k_{\mathrm{B}}T}}\exp\left(\frac{\delta\mu_{\mathrm{l-ERS},i}}{k_{\mathrm{B}}T}\right) \tag{12}$$

where $f_{\mathrm{i},\perp} = f_{\mathrm{b,i},\perp} + f_{\mathrm{v,i},\perp}$ is the effective impinging flux of group i. For typical growth conditions where $f_{\mathrm{V}} > f_{\mathrm{III}}$, the vapour pressure of group V can be assumed to be proportional to the incoming flux, $f_{\mathrm{v,V}} \propto f_{\mathrm{b,V}}$. This is because a

[6] Even though the prefactors in principle could be derived analytically, it is a complex problem and will eventually involve estimations and simplifications for different entropy contributions and effective coordination numbers and they are therefore more reasonably used as fitting parameters.

huge contribution of the excess As species must come from secondary adsorption, see [23]. Secondary adsorption of group III can typically be neglected, although for growth on substrates covered with a thermally grown oxide layer it can play a significant role, as shown by Rieger *et al* [55]. The va and al transition flux can be written, respectively, as

$$\Delta\Gamma_{(\mathrm{vb})\mathrm{a},i} \cong f_{i,\perp} - \frac{\rho_i}{\rho_i^{\mathrm{ERS}}} \frac{p_{i_n}^{\mathrm{ERS}}}{\sqrt{2\pi m_{i_n} k_\mathrm{B} T}} \exp\left(\frac{\delta\mu_{a-\mathrm{ERS},i}}{k_\mathrm{B} T}\right), \tag{13}$$

$$\Delta\Gamma_{\mathrm{al},i} = \Xi'_{\mathrm{la},i} \exp\left(-\frac{\delta h_{\mathrm{la},i}^{\mathrm{TS,ERS}}}{k_\mathrm{B} T}\right) \times \left(\frac{\bar{\rho}_i}{\bar{\rho}_i^{\mathrm{ERS}}} x_i^{\mathrm{ERS}} \exp\left(\frac{\delta\mu_{a-\mathrm{ERS},i}}{k_\mathrm{B} T}\right) - x_i \exp\left(\frac{\delta\mu_{\mathrm{l}-\mathrm{ERS},i}}{k_\mathrm{B} T}\right)\right). \tag{14}$$

Finally, the net sorption currents (equation (11)) are given as

$$\begin{aligned} I_{(\mathrm{vb})\mathrm{l},i} &= \int \Delta\Gamma_{(\mathrm{vb})\mathrm{l},i}\, \mathrm{d}A_{\mathrm{vl}} \\ &\cong A_{\mathrm{vl}} \left(f_{\mathrm{v},\perp} - \frac{x_i}{x_i^{\mathrm{ERS}}} \frac{p_{i_n}^{\mathrm{ERS}}}{\sqrt{2\pi m_{i_n} k_\mathrm{B} T}} \exp\left(\frac{\delta\mu_{\mathrm{l}-\mathrm{ERS},i}}{k_\mathrm{B} T}\right)\right) \\ &\quad + A'_{\mathrm{vl}} f_{\mathrm{b},i}, \\ I_{\mathrm{al},i} &= \int \Delta\Gamma_{\mathrm{al},i}\, \mathrm{d}A_{\mathrm{vl}} \\ &\cong L_{\mathrm{TL}}\, \Xi_{\mathrm{al},i} \left(\bar{\rho}_i - \bar{\rho}_i^{\mathrm{ERS}} \frac{x_i}{x_i^{\mathrm{ERS}}} \exp\left(\frac{\delta\mu_{\mathrm{l}-\mathrm{ERS},i}}{k_\mathrm{B} T}\right)\right). \end{aligned} \tag{15}$$

In equation (15) all information about the transition state barriers from the l to the v or a states is stored in the ERS parameters, due to the detailed balance assumption at equilibrium. Only a given projection of the liquid surface A'_{vl} is exposed to the incident beam flux, depending on the beam direction and droplet geometry [57]. L_{TL} is the length of the TL. Note that if $\delta g_{lq,i}^{\mathrm{TS,ERS}} < \delta\mu_{\mathrm{l}-\mathrm{ERS},i}$, the exponentials vanish in equation (15) according to equation (7).

To get a more intuitive feeling of the effect of growth conditions on the adatom kinetics in terms of an effective diffusion length, adatom migration on a large homogeneous planar interface serves as a good example [56]. Even though this approach is not accurate for modelling the growth dynamics, it is instructive and intuitive, and sufficient to understand many overall growth phenomena as function of growth conditions. There are three main transition paths for an adatom, namely surface diffusion (aa), desorption (av) and incorporation (as). Using the TS approach, See section A.1 in the appendix, the diffusion length of an adatom on a surface j can be written as

$$\lambda_{j,i} \cong \left[\bar{Z}'_{\mathrm{aa},i} l_{\mathrm{a},i}^2 \exp\left(-\frac{\delta h_{\mathrm{aa},i}^{\mathrm{TS,ERS}}}{k_\mathrm{B} T}\right)\left(\bar{Z}'_{\mathrm{as},i} \exp\left(\frac{\delta\mu_{\mathrm{a}-\mathrm{ERS},i}}{k_\mathrm{B} T}\right) + \bar{Z}'_{\mathrm{av},i} \exp\left(-\frac{\delta h_{\mathrm{av},i}^{\mathrm{TS,ERS}}}{k_\mathrm{B} T}\right)\right)^{-1}\right]^{1/2}, \tag{16}$$

where we assume that $1 - \bar{\rho}_{j,i} \approx 1$, and that the density of incorporation sites is given as $\bar{c}_{\mathrm{inc,III(V)}} \propto \exp(\delta\mu_{\mathrm{a}-\mathrm{ERS},i}/k_\mathrm{B} T)$. $l_{\mathrm{a},i}$ is the lattice site spacing and the entropy change is included in the prefactors, $\bar{Z}'_{pq,i} = \bar{Z}_{pq,i} \exp(\delta s_{pq.i}/k_\mathrm{B})$. In figure 5 we show estimations of diffusion lengths as a function of growth conditions, using parameters given in section A.3 in the appendix.

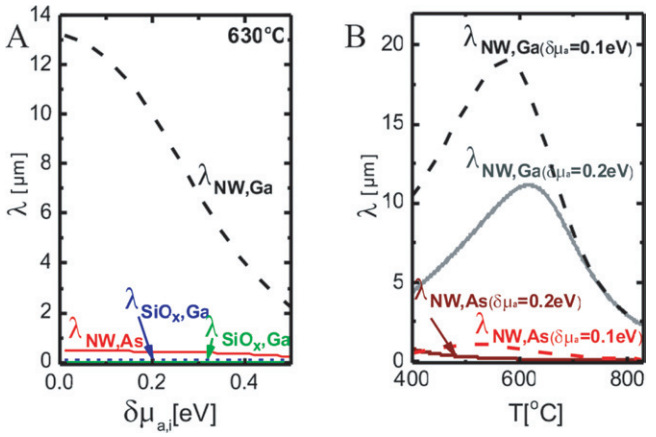

Figure 5. Diffusion length estimations for uniform diffusion of Ga and As on the NW sidefacets and thermal oxide at $T = 630\,^{\circ}\mathrm{C}$, using activation enthalpies listed in section A.3 in the appendix. It is seen that on the oxide surface the diffusion length is independent of the chemical potential because it is in the desorption limited regime where the chemical potential does not play a role according to equation (16). But the diffusion length for Ga adatoms on the crystalline facets (here (1 1 0) sidefacets) depends very strongly both temperature and chemical potential, See section A.1 in the appendix.

Above we have treated the static case of adatom diffusion. An approach to treat the dynamics of adatom diffusion and the adatom collection to the liquid phase is discussed in detail in section A.2 in the appendix, where we show how to merge a 'Dubrovskii/Johansson' static diffusion scheme into the dynamic formalism using the TS kinetics with a uniform diffusivity along NW and substrate, a method which is used for the modelling in section 3.

2.2. *The liquid–solid phase transition*

We now turn to the actual crystal formation at the ls interface. Here, we will for simplicity assume that the liquid diffusion is fast on the time scale of NW growth, and that the liquid phase is homogeneous. The dynamic treatment including non-homogeneous liquids can be carried out if a reference composition and liquid diffusivity are known. See for example [57, 58] for treatment of non-homogeneous liquids. The possibility of fast diffusion along the growth interface during VLS is assumed negligible, as indicated by a study by Dick *et al* [59]. As shown by Schwarz and Tersoff [45], if the solid were isotropic, the equilibrium shape would be with a curved ls interface. But as the authors also pointed out in a later publication, in the anisotropic case (which is relevant for III–V NW growth), the morphology is strongly faceted [46]. It is complicated to treat the dynamical evolution if the solid is partially wetted by a droplet which at the same time is changing in size during growth. For such a system the preferential orientations of the facets depends on the liquid phase size and it is necessary to describe the crystal growth in terms of both facet sizes and facet orientations (and

therefore an independent parameter set $\{X\}$ of both 'areas' and 'orientations', as explained in section 2.1). An additional complication affects the evolution of the crystal shape if the facets are limited in their growth rate by the formation of a small nucleus [60], see section 2.3 for a treatment of the nucleation limited axial growth at the topfacet. For VLS growth one only considers growth at the ls interface and distinguishes between two types of ls transitions:

Nucleation free growth. Facets which are limited in their growth rate or in their change of orientation by the transfer of single pairs to the growth front, as described by equation (9).

Nucleation limited growth. Facets which are limited in their growth rate by the formation of a small nucleus, or more generally limited in their change of X due to an energy barrier which is larger than the single pair transition state barrier.

As in [26], the ls growth system will be divided into two main regimes (mainly due to traditional reasons as explained below).

Regime I. The TL stays in contact with the topfacet.

Regime II. The TL is not in contact with the topfacet, or possibly only for a short time during a nucleation event at the topfacet.

The vast majority of literature on the nucleation at the topfacet has assumed an ideal regime I, where the ls interface is perfectly flat, see for example [25]. However, it is very uncertain under which material systems and growth conditions ideal regime I conditions applies. It is likely that it is only relevant under non-steady-state conditions where the liquid decreases significantly in size, such as immediately after closing the shutter of the group III source or upon during cool down where the nucleation barrier is lowered [27]. But as recent in-situ TEM experiments [40–42] strongly suggests and as shown in the modelling examples in section 3.5, regime II may be a dominant VLS steady-state growth mode.

Many studies suggest that the dominating type of growth at the topfacet is strongly nucleation limited (see for example [62]) while small truncation facets at the edges of the growth interface might be nearly nucleation free [40, 41]. The chemical potential of the solid depends on the stacking type of the crystal structure (e.g. s: WZ(2H), ZB(3C), 4H, 6H, etc), with ZB and WZ being the most common sequences, where the ZB structure has the lowest cohesive energy for most III–V's and are therefore favoured in bulk materials [61, 62]. The liquid needs to reach a critical level of supersaturation (typically of the order of a few hundred meV per III–V pair) [25] before the nucleation barrier at the topfacet can be overcome. Under this constraint other facets which are not nucleation limited will reshape in respond to the elevated liquid chemical potential at a rate determined by equation (9), and the whole growth system is therefore in a configuration far from equilibrium. For VLS growth, group V is typically the less abundant specie in the liquid, i.e. $x_{\mathrm{III}} > x_{\mathrm{V}}$. For a fixed solid stoichiometry, the activation energy for the nucleation free single pair ls transitions, equation (9) can be written as

$$\Delta\Gamma^{X}_{\mathrm{ls,III-V}} = \Xi_{\mathrm{ls,III-V}} \exp\left(-\frac{\delta g^{\mathrm{TS,ERS}}_{\mathrm{ls,III-V}}}{k_{\mathrm{B}}T}\right) \times \left(x_{\mathrm{V}} \exp\left(\frac{\delta\mu_{\mathrm{l-ERS,III-V}}}{k_{\mathrm{B}}T}\right) - x^{\mathrm{ERS}}_{\mathrm{V}} \times \exp\left(\frac{\delta\mu^{X}_{\mathrm{s-ERS,III-V}}}{k_{\mathrm{B}}T}\right)\right). \quad (17)$$

As the liquid chemical potential $\delta\mu_{\mathrm{l-ERS,III-V}}$ is an oscillating function due to the nucleation limited growth at the topfacet [62], the parameter X (describing nucleation free facet size or angle) will therefore oscillate accordingly. Because the chemical potentials depend on location and system morphology, so do the transition fluxes, and the free energy minimization needs to be described with respect to an appropriate set of independent parameters, $\{X(\omega)\}$. Generally speaking, the larger the parameter set the more accurately the modelling, but also the more computations are needed. In three dimensions, the chosen set of parameters $\{X(\omega)\}$ will depend on ω which is defined to be the angle between the middle of the sidefacet and position as measured from the centre of the top facet, see [26] for clarification.

As shown in the stereographic projection in figure 6(*a*), if only considering ZB and WZ stacking, it is sufficient to divide the ω-dependence of the crystal into three sections because the ZB crystal structure has three-fold symmetry. The WZ crystal structure has six-fold symmetry around the growth axis and is therefore also described completely within this region. In table 1 in section A.3 in the appendix, we give the interfaces with lowest energies for the ZB and WZ structure (we restrict ourselves to the upper half hemisphere with polar (1 1 1) ZB or [0 0 0 1] WZ directions). To describe the NW diameter as a function of ω in terms of the cross sectional Wulff shape[7], we need to look at the energies of the facets in the $\theta = 90^{\circ}$ plane (the outer ring) in the stereographic projection in figure 6(*a*). For a cross sectional six-fold symmetric NW it is enough to describe the NW diameter at the growth interface in the range $\omega = [-30^{\circ} : 30^{\circ}]$ as

$$d_{\mathrm{NW}}(\omega) = \frac{d_{\mathrm{NW}}(\omega = 0^{\circ})}{(1 + \omega\eta(\omega))\cos(\omega)}, \quad (18)$$

where the function $\eta(\omega)$ determines the cross sectional shape of the growth interface. $\eta(\omega)$ is a complicated function that depends on many factors. We can simplify it as $\eta(\omega) = \eta_0(\cos^{-1}(\omega) - 1)\omega^{-1}$, where $\eta_0 = 0$ for complete hexagonal facetting and $\eta_0 = 1$ in the isotropic case (complete axi-symmetric cross section). In the case of the ZB structure which has a three-fold symmetric crystal structure, it is very likely that the NW cross section does not have a perfect six-fold geometrical symmetry. In this case we need to take account of the possibility of a three-fold symmetric cross section where the diameter is given by $d_{\mathrm{NW}}(\omega) = r_{+}(\omega) + r_{-}(\omega)$ with $r_{+}(\omega)$

[7] The Wulff shape is the shape of a crystal with the lowest free energy possible for a given crystal volume. See textbooks on crystal growth for a more detailed explanation.

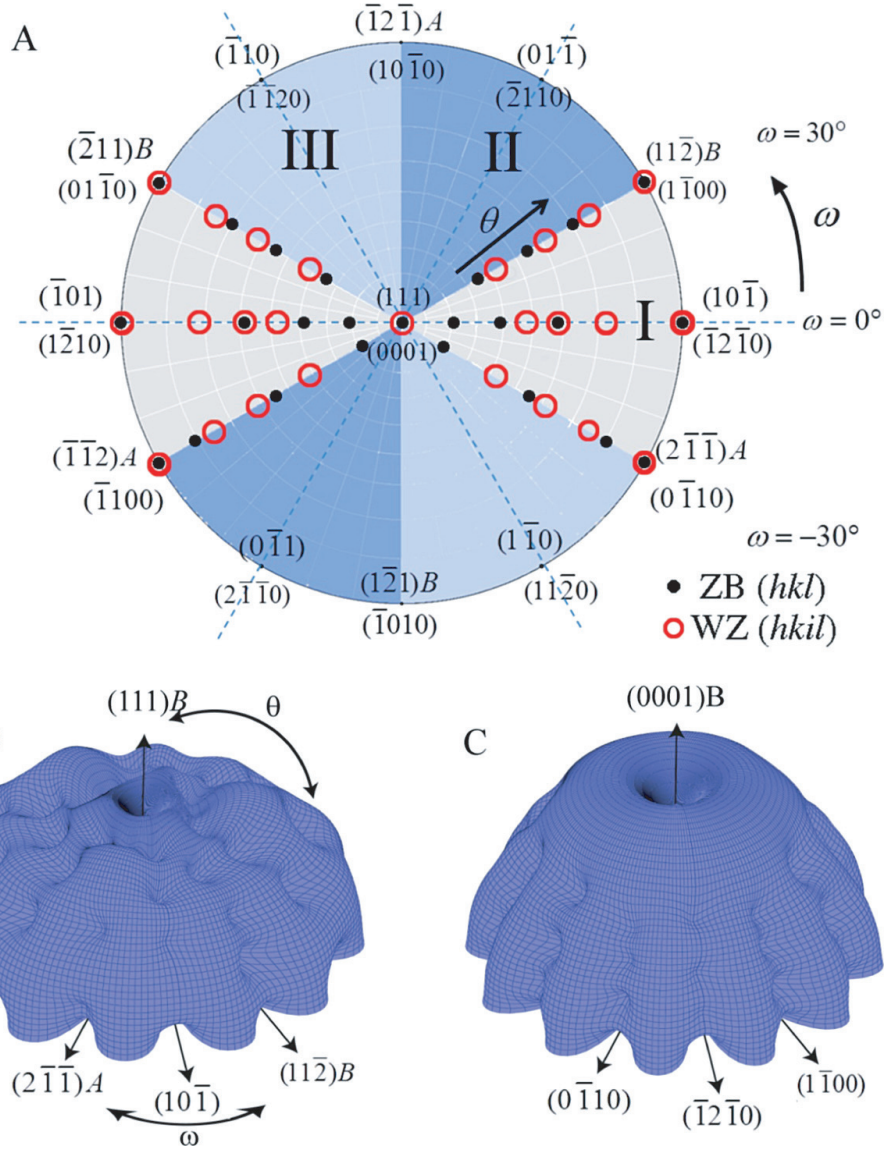

Figure 6. III–V NW crystal anisotropy for ZB and WZ structures. (*a*) A stereographic projection of the upper hemisphere along the [1 1 1] ([0 0 0 1]) zone axis of a ZB (WZ) crystal. Due to the three-fold symmetry of the ZB structure along (1 1 1), we only need to consider the grey areas, which are described in the range $\omega = [-30°; 30°]$. The black dots represent the facet normals $(h\,k\,l)$with the highest symmetry (with typically the lowest predicted interfacial energy) of the ZB structure and the red rings represent the corresponding facets $(h\,k\,i\,l)$ of the WZ structure. The edge of the projection represents the plane normal's perpendicular to the growth axis, $\theta = 90°$. Lower hemisphere orientations are found by mirroring the upper hemisphere orientations in the zone axis and change sign of the miller indices. The specific angles shown are given in section A.3 in the appendix. 3D gamma plot in spherical coordinates (θ, ω) of the anisotropic ls interface energy for (*b*) ZB and (*c*) WZ structure using equation (20) with the three lowest miller index facets in the 12 directions between the (1 1 1) growth direction and $\{1\ -1\ 0\}$ or $\{1\ 1\ -2\}$ families (see section A.3 in the appendix). The distance between origo and the surface is proportional to the interface energy of the given orientation.

and $r_-(\omega) = r_+(\omega + 180°)$ being the radius as measured from the centre of the NW crystal. For complete facetting ($\eta_0 = 0$) and a constant NW volume, the relation between r_- and r_+ is:

$$r_+ = 2r_- - \sqrt{3r_-^2 - 2\sqrt{3}\cdot A_c}, \tag{19}$$

where A_c is the cross sectional area. According to Wulff, in the absence of a liquid phase, the cross sectional equilibrium shape of the NW crystal would be given by $\gamma_A/\gamma_B = r_+/r_-$, where $\gamma_A(\gamma_B)$ is the effective vertical surface energy of the facet normal to the $r_-(r_+)$ vector.

For a more complete description of the dynamics we need the values of the anisotropic surface and interface energies for the different crystal structures. To carry out the iterative minimization of the free energy are desirable. To this end, we need a γ plot with rounded cusps that can approach arbitrarily close to the sharp cusps of faceted orientations. This can be realized by summing a set of 2D Lorentzian functions centred on the facets of high symmetry, which have the lowest interface energies. The angular dependence of the interface energy is then described, in angular coordinates (θ, ω), by

$$\gamma_{vs,j}(\theta, \omega) = \gamma_{vs0} - \sum_{h\,k\,l} c_{h\,k\,l} \frac{I_{h\,k\,l}}{1 + (\phi_{h\,k\,l}(\theta, \omega)/w_{h\,k\,l})^2}, \tag{20}$$

where $\phi_{h\,k\,l}(\theta,\omega) = \arccos(\cos(\theta-\theta_{h\,k\,l}) + \sin(\theta)\sin(\theta_{h\,k\,l})(\cos(\omega-\omega_{h\,k\,l})-1))$ is the angle between the facet $h\,k\,l$ (see table 1) and direction (θ,ω), where $\theta = 0$ corresponds to the growth direction (see figures 6(*b*) and (*c*) for ZB and WZ structure).

In equation (20), the maximum interface energy is noted γ_{vs0}, and the decrease in interface energy at each high symmetry facet is given by the 'intensity' $\mathrm{I}_{h\,k\,l} = \gamma_{\mathrm{vs0}} - \gamma_{\mathrm{vs},j}$. The values of $\gamma_{\mathrm{vs},j}$ for the main orientations can either be found in the literature or obtained from density functional theory calculations. $w_{h\,k\,l}$ is a scale parameter which specifies the half-width at half maximum of the energy increase around the $(h\,k\,l)$ facet. $c_{h\,k\,l}$ is a constant close to unity, but if $w_{h\,k\,l}$ is large the interface energy may have to be adjusted to a value slightly lower than unity because the contributions from adjacent facets may overlap. We will simply assume that the ls interface energy is given by $\gamma_{\mathrm{ls}}(\theta,\omega) = \sigma\gamma_{\mathrm{vs}}(\theta,\omega)$, where σ is typically assumed to be a constant of the order 0.3–0.5.

2.3. Nucleation limited axial growth in the (1 1 1)/(0 0 0 1) direction

We will here treat the nucleation limited growth which takes place at the ls top facet separately because this is where the axial growth and where the final crystal structure of the NW is formed. Many recent experimental studies have indicated that growth on the dominating ls (1 1 1)/(0 0 0 1) top facet is limited by the formation of a nucleus, which means that the liquid supersaturation needs to exceed a certain critical value before a new monolayer can be formed, see for example [39, 63]. This implies that the topfacet is stabilized as long as the difference in chemical potentials between the liquid and topfacet is smaller than a critical value, due to large activation energies both ways. Because the mother phase (the liquid) is small, the liquid supersaturation drops far below the critical level after a ML formation and probability of having a subsequent second nucleation is unlikely. We are therefore only interested in single nucleation events. To describe the probability of forming a critical nucleus we need to take account of the stochastic nature of the phase fluctuations which causes nucleation. But first, we need an expression for the mean nucleation rate.

If the movement of atoms in and out of clusters of various sizes (smaller than the critical nucleus) at the growth interface, takes place on a timescale much smaller than the time between nucleation events, the nucleation probability can be derived assuming steady-state nucleation rate conditions [64–66], which is the typical assumption in NW growth theory [10, 19, 20, 25]. It is reasonable to assume that the attachment/detachment frequency of III–V pairs to and from the clusters on the (1 1 1)B topfacet is limited by the group V elements. This is not only because the concentration of group V is low in the liquid but also because the group III elements are attached with only one covalent bond on average in the 'B' terminated surface when group V is absent. Once group V is present, the pair is stabilized leaving only one free covalent bond per pair on average (reconstruction is not considered in the continuum formalism). With this, the mean nucleation rate at given site with coordinates (r,ω) at the topfacet (r measured from the centre) can then be written as

$$j_{\mathrm{s}(r,\omega)} = A_{n^*} Z_{\mathrm{s}(r,\omega)} c_1 \Xi_{\mathrm{ls,III-V}} x_{\mathrm{V}} \exp\left(-\frac{\delta g^{\mathrm{TS,ERS}}_{\mathrm{ls,int}}}{k_{\mathrm{B}}T}\right) \times \exp\left(-\frac{\Delta G_{n^*,\mathrm{s}(r,\omega)}}{k_{\mathrm{B}}T}\right), \tag{21}$$

where A_{n^*} is the step area of the critical nucleus of n^* pairs, $Z_{\mathrm{s}(r,\omega)} = 1/n^*\sqrt{\Delta G_{n*,\mathrm{s}(r,\omega)}/4\pi kT}$ is the 2D Zeldovich factor and $\Delta G_{n*,\mathrm{s}(r,\omega)} = -\sum_{i=2}^{n^*}(\delta\mu_{1-\mathrm{ERS,III-V}} - \delta\mu^i_{\mathrm{s}(r,\omega)-\mathrm{ERS,III-V}})$ is the formation free energy of the nucleus, with $\delta\mu^i_{\mathrm{s}(r,\omega)-\mathrm{ERS,III-V}}$ being the chemical potential of a cluster of i pairs at (r,ω). s denotes solid structure described by its stacking type (ZB (3C), WZ (2H), 4H , etc). Consistent with transition state approach described above, the forward flux from the liquid to the cluster, $\Gamma_{\mathrm{ls,III-V}}$, is assumed independent of the size of the cluster, (the backward flux from the clusters depends on the cluster size but cancels out in the derivation). $\delta g^{\mathrm{TS,ERS}}_{\mathrm{ls},int}$ is the transition state barrier for attachment of a single pair to the clusters at the interface. The detailed kinetics at the interface is unknown; we thus simply assume that the concentration of single III–V pairs attached to the interface c_1 (single pair clusters) is equal to the concentration of the group V in the liquid, $c_1 \approx x_{\mathrm{V}}$. Once the nucleation event has occurred, the ML is completed in a non-nucleation limited manner, at a rate given by equation (17), and the liquid supersaturation builds up slowly again until the next nucleation event takes place.

The nucleus formation free energy can be written as in a more familiar form,

$$\Delta G_{n^*,\mathrm{s}(r,\omega)} = -\Delta\mu^{\infty}_{\mathrm{ls,III-V}} n^* + h\sum_{k=1}^{m} l_k \gamma_{\mathrm{step}(r,\omega),k}, \tag{22}$$

where the first term is the formation free energy required to form the volume part of the nucleus. The second term is the excess free energy due to the formation of a dividing step. $\gamma_{\mathrm{step}(r,\omega),k}$ and l_k are the free energy and length of the kth step facet, respectively. As the nucleation takes place when the number of pairs in the cluster exceeds the critical value, $n \geqslant n^*$, which is associated with the maximum free energy increase given by the condition,

$$\frac{\mathrm{d}\Delta G_{n^*,s(r,\omega)}}{\mathrm{d}n} = -\Delta\mu^{\infty}_{\mathrm{ls,III\text{-}V}} + h\sum_{k=1..m}\left(\frac{\mathrm{d}l_k}{\mathrm{d}n}\gamma_{\mathrm{step}(r,\omega),k} + l_k\frac{\mathrm{d}\gamma_{\mathrm{step}(r,\omega),k}}{\mathrm{d}n}\right) = 0 \tag{23}$$

we can derive an explicit expression for the nucleation barrier ΔG^*_n by extracting n^* from equation (23) (l_k depends on n^*) and insert it into equation (22). The last term in the summation of equation (23) is typically neglected in continuum models, as the interface energies are assumed constant as a function of interface area.

For regime II we will divide all the possible nucleation sites into three main classes (see figure 7).

(A) At the edge between the topfacet and truncated facet, see [42]. Here the nucleus forms an extension to the truncated

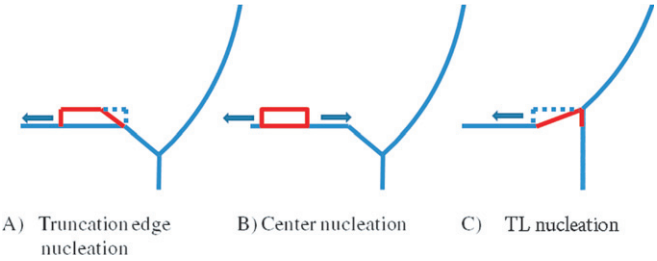

Figure 7. Cross section view on the triple line region at a given ω, showing three different ways to form an energetically favourable step on the topfacet. (*A*) A step formed due to a nucleation event at the corner between the topfacet and a truncated facet, a regime II type nucleation. (*B*) A step formed due to a nucleation event at the centre of the top facet. (*C*) If the relative droplet size is sufficiently small and/or the liquid supersaturation is sufficiently high at nucleation, it is possible that the truncation size becomes positive which will induce a TL nucleation event at the topfacet and the necessary step for step flow is formed.

facet a crystal structure different from the equilibrium bulk structure can be dictated by the orientation of this facet (similarly to what was proposed in the case of a nucleus in contact with a vapour by Glas *et al* [25]).

(B) Nucleation at the centre of the top facet, see for example [19]. The preferential crystal structure here is the structure with the lowest cohesive energy which is typically ZB [67].

(C) It is possible that the truncation size becomes positive at a given ω, before one to the other types of nucleation events takes place. Then a TL nucleation event will be induced at the topfacet and the necessary step for step flow is formed. A fast completion of the monolayer will lower the supersaturation and move the truncation back to negative values (provided that the barrier of forming the truncation facet is small enough). For a six-fold crystal geometry it is likely that such an event will take place at the corners, i.e. $\omega = 30^\circ$. If the liquid size is decreasing TL nucleation becomes more and more dominant and the system will eventually move into regime I.

Under conditions where the time needed to reach steady-state composition in the liquid is smaller than the time between the formation of two consecutive MLs, the total centre-nucleation rate can be written as $J_c \cong 2\pi j_c \int_{\text{Center}} ((d_{\text{NW}}(\omega)/2) - \Delta z(\omega)\tan(\theta_T(\omega)) - l_m^*)\,\mathrm{d}\omega$, where $\Delta z(\omega)\tan(\theta_T(\omega))$ is the decrease in topfacet length at ω due to the truncation. For truncation edge nucleation we will integrate over the part with a negative truncation, $J_T \cong \pi \int_{l_T} l_m^*(\omega)(d_{\text{NW}}(\omega) - \Delta z(\omega)\tan(\theta_T(\omega)))\, j_T(\omega)\,\mathrm{d}\omega$. In order to carry out a more realistic modelling of the s-stacking probabilities we can account for the stochastic nature of nucleation by multiplying equation (21) by a random number between 0 and 1, $\Re(0, 1)$, at each time step, and define a normalized value δ above which nucleation will take place

$$\int_{\text{Topfacet}} j_{s(r,\omega)}\,\mathrm{d}A_{\text{topfacet}} \cdot \Re(0, 1) \geqslant \delta. \qquad (24)$$

Finally, whenever one or more sites fulfil equation (24) the rate of the subsequent step flow and completion of a ML are determined by equation (17). However it is possible that the truncation $(\Delta z(\omega)\tan(\theta_T(\omega)))$ under certain conditions goes to zero and at certain positions becomes positive before equation (24) is fulfilled (figure 7(*c*)). In this case a step is naturally provided at the triple line (TL) and completion of a monolayer will take place at the same time as the truncation most likely goes to negative again due to a lowering of the liquid supersaturation.

3. Dynamical modelling examples of self-catalysed GaAs NW growth

In this section we will show examples of how to use the theoretical formalism (presented in section 2) to analyse and understand the dynamics of self-catalysed GaAs NW growth. We start with analyses of the evolution of the overall morphology of self-catalysed GaAs NW growth on Si substrates (sections 3.1–3.4).

3.1. Calculating the ERS and size effects for self-catalysed GaAs NW growth simulations in the axi-symmetric approximation

To simulate a specific process such as self-catalysed GaAs NW growth on Si (1 1 1) substrates, requires the relevant ERS parameters and size effects based on the assumptions made for the simulation. Thus, before giving detailed simulation examples of the overall NW growth, we will first go through the specific calculations needed for this system. As mentioned, modelling the overall morphology does not require detailed information on the shape of the ls interface, and in this section we will therefore assume an axi-symmetric cross section (ω dependence can be neglected) and an ideal regime I with a single flat ls interface. In this case we do not need to define an independent parameter set, but only use the liquid size evolution and nucleation at the topfacet to determine the evolution of the crystal morphology in terms of the diameter d_{NW} at the growth interface and the vl contact angle θ with respect to the topfacet. The size effect terms in equation (5) and (6) for the chemical potential can be found using the trigonometric relations,

$$A_{\text{ls}} = \frac{\pi d_{\text{NW}}^2}{4}, \qquad A_{\text{vl}}(\theta) = \frac{\pi d_{\text{NW}}^2(1 - \cos(\theta))}{2\sin^2(\theta)}$$

and

$$N_{\text{l}}(d_{\text{NW}}, \theta) = \frac{\pi d_{\text{NW}}^3}{24\Omega_{\text{l}}} \frac{(1 - \cos(\theta))^2(2 + \cos(\theta))}{\sin^3(\theta)},$$

where Ω_{l} is the atomic volume in the liquid. A change in d_{NW} implies not only a change in the ls and vl areas but also the formation of a new vs area corresponding to the absolute change in the ls area. We have not taken account here of the possibility of wetting the sidefacets for a cylindrical shaped cross section, as described in [68, 69]. For a detailed analysis of the wetting in regime I (i.e. on a flat hexagonal top facet) see [26]. To calculate the chemical potentials of the ERS (equation (1)), we need to calculate the liquid chemical

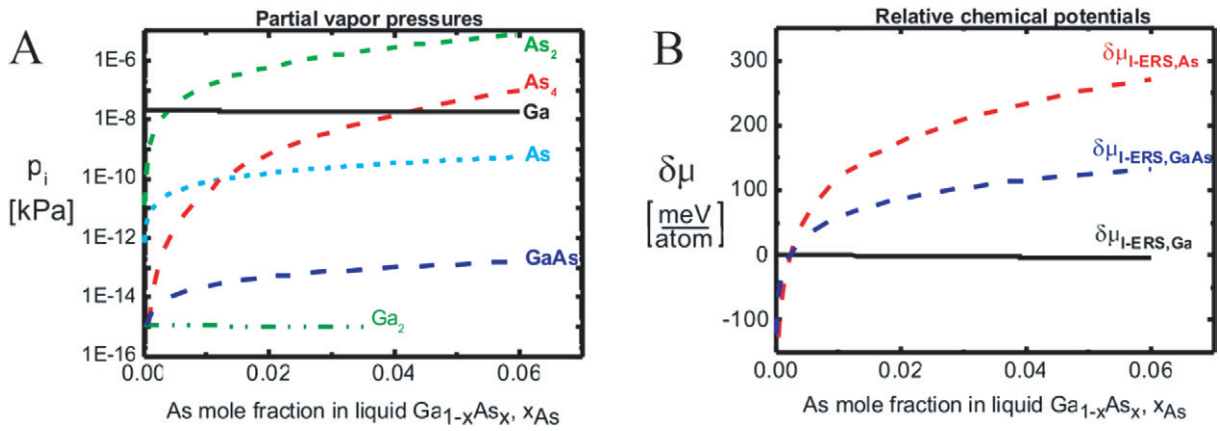

Figure 8. Partial vapour pressures (*a*) and relative liquid chemical potentials (*b*) of the relevant species in the liquid Ga-assisted case for GaAs NW growth, as a function of the As mole fraction at $T = 630\,^{\circ}\mathrm{C}$. The critical value $\delta\mu^{c}_{\mathrm{l-ERS,III-V}}$ is typically of the order 100 meV per atom which corresponds to few per cent of As in the liquid as shown in (*b*). The As concentration is kept low in the liquid due to the fast increasing vapour pressure of As_2, and there exists a certain threshold value of beam flux/vapour pressure where the steady-state concentration of As in the liquid exceeds the critical value for nucleation at the topfacet.

potentials when the liquid phase is in equilibrium with the solid. For liquid binaries (self-assisted growth), the chemical potential is given by the tangent method, or correspondingly;

$$\mu^{\infty}_{\mathrm{l},i}(x_{\mathrm{V}}, T) = g^{\infty}_{\mathrm{l}}(x_{\mathrm{V}}, T) + (1 - x_i)\frac{\partial g^{\infty}_{\mathrm{l}}(x_{\mathrm{V}}, T)}{\partial x_i}. \qquad (25)$$

Here the liquid free energy per atom of an infinitely large binary alloy is given by $g^{\infty}_{\mathrm{l}}(x_{\mathrm{V}}, T) = (1-x_{\mathrm{V}})g_{\mathrm{l,III}}(T) + x_{\mathrm{V}}g_{\mathrm{l,V}}(T) + g_{\mathrm{l,mix}}(x_{\mathrm{V}}, T)$ where $g_{\mathrm{l,mix}}(x_{\mathrm{V}}, T) = (1 - x_{\mathrm{V}})x_{\mathrm{V}}[L_0(T) - L_1(T)(1 - 2x_{\mathrm{V}})] + RT[(1 - x_{\mathrm{V}})\ln(1 - x_{\mathrm{V}}) + x_{\mathrm{V}}\ln(x_{\mathrm{V}})]$ accounts for the asymmetry in the compositional effect on the free energy by using the Redlich–Kister formalism [70] as in [71] with two liquid interaction parameters L_0 and L_1. These parameters together with the free energy values of the pure components $g_{\mathrm{l},i}$ are given for $g_{\mathrm{Ga}_{1-x_{\mathrm{V}}}\mathrm{As}_{x_{\mathrm{V}}}}$ and $g_{\mathrm{In}_{1-x_{\mathrm{V}}}\mathrm{As}_{x_{\mathrm{V}}}}$ in table 2 of section of A.3 in the appendix, where the equilibrium concentrations are estimated from fitting the liquidus values reported in [87]. All Gibbs free energies and chemical potentials are relative to the enthalpy of the standard element reference (HSER_i)[75], and denoted $g'_{\mathrm{l}}(T)$ and $\mu'_{\mathrm{l},i}(T)$, respectively. Using these data, the ERS chemical potential $\mu^{\mathrm{ERS}'}_i = \mu^{\infty'}_{\mathrm{l},i}(x^{\mathrm{ERS}}_{\mathrm{V}}, T)$ is calculated using equation (25) and the relative chemical potential is simply $\delta\mu_{\mathrm{l},i}(x_{\mathrm{V}}, T) = \mu'_{\mathrm{l},i}(x_{\mathrm{V}}, T) - \mu^{\mathrm{ERS}'}_i$.

To calculate the partial vapour pressures over a liquid of given composition, we note that $\mu'^{n}_{\mathrm{v},i_n} = n\mu'_{\mathrm{l},i}$, where n is the number of atoms in the molecule considered and $'^{n}$ denotes that the value is given with respect to n times the standard reference. Using the thermodynamic data from appendix 2 in [75], we find an expression for the Gibbs free energy of a pure i_n species, $g^{\mathrm{pure}'^{n}}_{\mathrm{v},i_n}(T) = \Psi'^{n}_i(T) + RT\ln(P)$, where P is the total pressure and $\Psi'^{n}_i(T)$ is a function of temperature only (see table 3 in section A.3 in the appendix for the thermodynamic data). Now, since $\mu'^{n}_{\mathrm{v},i_n} - \mu^{\mathrm{pure}'^{n}}_{\mathrm{v},i_n} = RT\ln(p_{i_n}/P)$, where $\mu^{\mathrm{pure}'^{n}}_{\mathrm{v},i_n} = g^{\mathrm{pure}'^{n}}_{\mathrm{v},i_n}$, we can write the following expression for the vapour pressure of element i_n:

$$p_{i_n}(x_{\mathrm{V}}, T) = \exp\left(\frac{n\mu'_{\mathrm{l},i}(x_{\mathrm{V}}, T) - \Psi'^{n}_i(T)}{RT}\right). \qquad (26)$$

The corresponding ERS pressures are then found by setting $\mu'_{\mathrm{l},i}(x_{\mathrm{V}}, T) = \mu^{\mathrm{ERS}'}_i$.

From figure 8(*a*) we see that the only species that may have significant partial pressures are the Ga and As_2 species. As the liquid supersaturation increases (increasing x_{As}), the vapour pressure of Ga remains almost constant, which means that the desorption flux of Ga form the liquid is almost constant. This means that the vl and al transition fluxes for the Ga species are roughly independent of the supersaturation. On the other hand, as the supersaturation increases the desorption of the As species increases very strongly (note the log scale).

To complete the ERS description, we need to calculate the adatom densities, $\rho^{\mathrm{ERS}}_{\mathrm{NW},i}$ and $\rho^{\mathrm{ERS}}_{\mathrm{sub},i}$, which we do by using kinetics. For the adatom collection we follow the approach outlined in section A.2 in the appendix, and the ERS adatom densities are found using equation (36) under ERS conditions, where $\rho^{\mathrm{ERS}}_{\mathrm{NW},i}$ is calculated by setting $L_{\mathrm{NW}} \to \infty$ and $\Delta\Gamma_{\mathrm{al},i} \to 0$, and $\rho^{\mathrm{ERS}}_{\mathrm{sub},i}$ is found by setting $r \to \infty$, both under conditions of the calculated ERS beam fluxes found above. Using the parameters listed in section A.2 in the appendix, the ERS adatoms densities are $\rho^{\mathrm{ERS}}_{\mathrm{NW,Ga}}(T = 630\,^{\circ}\mathrm{C}) = 5.3 \times 10^{17}\,\mathrm{m}^{-2}$ and $\rho^{\mathrm{ERS}}_{\mathrm{NW,As}}(T = 630\,^{\circ}\mathrm{C}) = 0.16 \times 10^{17}\,\mathrm{m}^{-2}$.

Tuning the fitting parameters can be time consuming. The fitting values of the relevant prefactors and activation free energies for adatom desorption and incorporation used in the simulations presented below are given in section A.3 in the appendix. In order to use the diffusion lengths given by equation (16), we need estimates of the activation energies $\Delta g^{\mathrm{TS,ERS}}_{pq,i} = \Delta h^{\mathrm{TS,ERS}}_{pq,i} - T\Delta s^{\mathrm{TS,ERS}}_{pq,i}$. As the entropy change as a function of temperature is negligible compared to the enthalpy change, we include the entropy contribution into the temperature independent prefactors as $\bar{Z}'_{\mathrm{as},i} = \bar{Z}_{\mathrm{as},i}\exp(\Delta S^{\mathrm{ERS}}_{pq,i}/k_{\mathrm{B}})$. This leaves us with enthalpy barriers which can be estimated from zero temperature ab initio calculations such as density functional theory methods [88]. After having built up the simulation framework, it can be used to analyse a variety of features and systems. Here, we will only give a few examples.

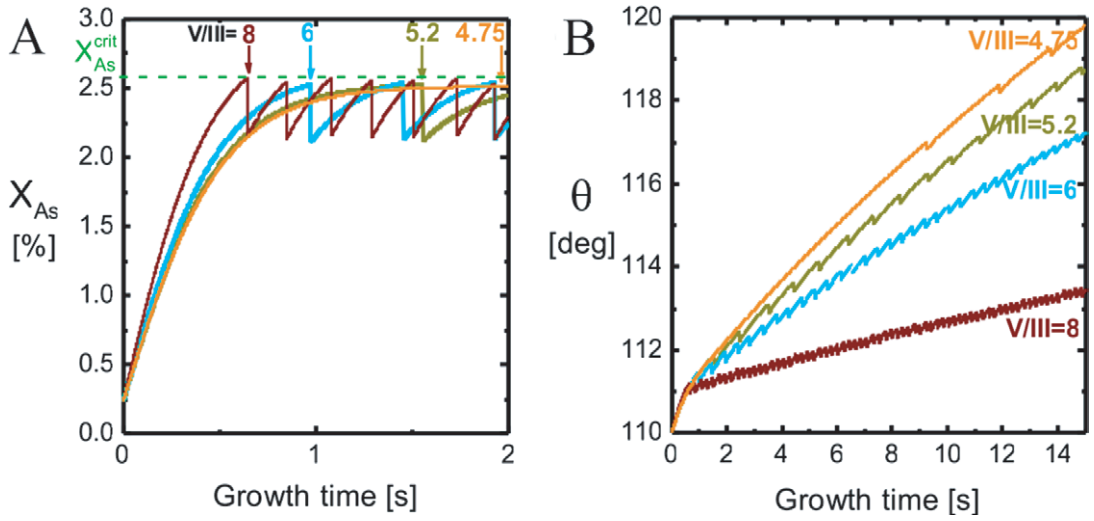

Figure 9. Initial transitory stage for the self-catalysed growth of GaAs NWs on Si(1 1 1) at $T = 630\,^{\circ}$C using a Ga flux equivalent to a planar growth rate of $GR_{planar} = 0.3\,\mu m\,h^{-1}$. The initial contact angle and NW diameter were set to $\theta_{initial} = 110^{\circ}$ and $d_{NW,0} = 50$ nm, and the time step was set to 0.001 s. (*a*) The As molar fraction in the $Ga_{1-x}As_x$ liquid phase and (*b*) contact angle just after opening the As shutter, are shown for four different V/III ratios close to the lower limit of the growth window. A fast drop in the curve corresponds to a nucleation event and the formation of one monolayer at the topfacet (for V/III = 4.75 it takes about 10 s before the first nucleation event takes place and for lower V/III ratios it becomes impossible overcome the nucleation barrier). This event lowers the liquid chemical potential $\delta\mu_{1-ERS,As}$ and $\Delta\Gamma_{vl,As}$ and $\Delta\Gamma_{al,As}$ immediately increase and forces the As molar fraction back to a level sufficient to overcome the nucleation barrier again.

3.2. Dynamics of self-catalysed GaAs NW growth on Si(1 1 1) at low V/III ratios

For typical MBE growth of self-assisted GaAs NWs on a Si (1 1 1) covered with a thin native SiO_x layer, Ga beam fluxes corresponding to planar growth rates of 0.1–0.3 $\mu m\,h^{-1}$ are commonly used, with a V/III flux ratio in the range 5–100 and a substrate temperature around $T = 630\,^{\circ}$C [72, 73]. There exists a certain 'growth parameter window', namely ranges of values for the basic growth parameters (temperature and beam fluxes), where it is possible to obtain NW growth (as a rule of thumb, the higher the temperature the higher the V/III ratio [22]). A general feature of the simulations is that there are sharp and well-defined boundaries for the growth parameter window. As the critical liquid supersaturation needed for nucleation at the topfacet is almost independent of the applied pressures (beam fluxes) [26], the axial growth rate is simply dictated by the time it takes for the liquid to reach the critical concentration of As, $\delta\mu_{1-ERS,As}^{crit}$, after being lowered upon a nucleation event and subsequent ML formation. If we neglect for simplicity the surface diffusion of As species and account for the impinging v states by simply using that the beam flux hits the total vl interface, the minimum As flux needed to obtain growth is roughly given as

$$f_{(bv)l,As,\perp}^{crit} \approx \frac{x_{As}^{crit}}{x_{As}^{ERS}} f_{lv,As}^{ERS} \exp\left(\frac{\delta\mu_{1-ERS,As}^{crit}}{k_B T}\right). \qquad (27)$$

Here x_{As}^{crit} is the critical concentration of As needed for a nucleation event and $f_{lv,As}^{ERS} \approx \sum_n p_{As_n}^{ERS}/\sqrt{2\pi m_{As_n} k_B T}$ is the flux of material evaporating from the liquid under ERS conditions. This means that the critical As flux is strongly dependent on the nucleation barrier and is only very little dependent on the Ga flux as long as there is a large liquid Ga phase. For the simulation shown in figure 9(*a*), the critical impinging As flux needed to overcome the nucleation barrier is roughly $f_{(bv)l,As,\perp}^{crit} \approx 100 \cdot f_{lv,As}^{ERS}$. To examine how the axial growth rate depends on the incoming fluxes, we need to look at the time it takes to refill the liquid phase after ML formation in order to recover the critical level. The outgoing lv flux of As depends on the liquid chemical potential roughly as $\Gamma_{lv} \propto (x_{As}/x_{As}^{ERS})^2$ (because $\delta\mu_{1-ERS,i}$ depends on the As concentration roughly as $\ln(x_{As}/x_{As}^{ERS})$). Now, because a small (large) droplet size will lead to a large (small) decrease in the As concentration immediately after a ML formation, the time needed to refill the liquid to the critical concentration depends on the droplet size. Thus, especially in the regions of the growth parameter window where the droplet size changes during growth, the incoming flux of Ga may also play an important role on the growth rate. In figure 9(*b*), it is seen that the droplet size increase at low V/III ratios, but as the V/III is increased the expansion of the droplet slows down as growth accelerates and Ga is incorporated faster into the NW. For moderate V/III ratios, where the droplet stays in a steady-state regime, the growth rate becomes more or less linear with the As flux until it reaches a limit where the droplet gets small and eventually gets consumed [74]. The apparent linear relation between NW length and As flux at moderate V/III ratios is consistent with previous reports [75]. At very high incoming As fluxes, As just consumes the droplet and NW growth becomes impossible.

In figure 10(*b*), a series of 6 min simulations shows an example of the huge change in morphology when changing the As_2 flux around the lower limit of the growth window. The NW diameter increase when the droplet reaches a size where the contact angle exceeds the wetting angle on the side walls. A higher V/III ratio implies less tapered NWs, because the droplet does not increase in size at the same speed as for lower V/III ratios (figure 9).

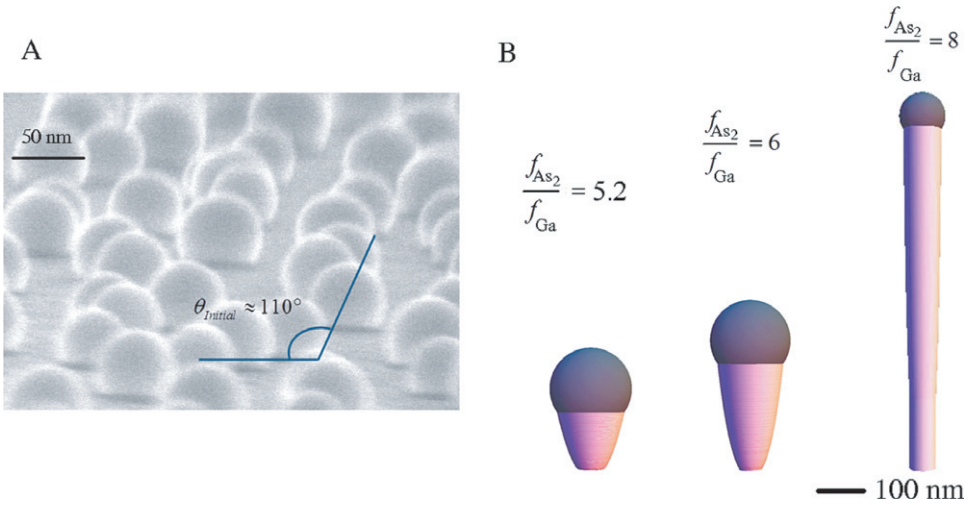

Figure 10. Around the lower limit of the V/III growth parameter window, a small change in the incoming As_2 beam flux may cause a big change in the NW morphology. (*a*) To estimate the initial contact angle and liquid size in the case of self-catalysed GaAs on Si(1 1 1) covered with a native oxide layer, Ga was deposited at the same initial conditions as before a typical NW growth (here 1 min of Ga pre-deposition) but without opening the valve to the As cell. These initial conditions were used for the simulations shown in figures 9(*a*) and (*b*). In (*b*) the same growth conditions as for the simulations shown in figure 9 have been used.

Figure 11. A TEM image of a GaAs NW grown for 40 min with a V/III ratio of 8 and a pyrometer temperature of 635 °C at $GR_{planar} = 0.3\ \mu m\ h^{-1}$. The distribution of TPs appearing at the bottom and at the tip is typical of Ga-catalysed GaAs NWs. The structural distribution depends on the relative size of the liquid phase (which changes during growth, see figure 12) because the latter has a huge influence on the nucleation statistics (see sections 2 and 4).

3.3. Relating the structure along the NW length to the relative size of the droplet

It is well known that it is generally possible to affect the crystal structure adopted by the NWs by tuning the growth conditions (for a review see [76]). In the case of self-catalysed GaAs NWs the preferential structure under quasi-steady-state growth conditions is typically ZB [77]. However, as shown by Jabeen *et al* [78] and Spirkoska *et al* [79] and many others, the density of twin planes (TPs) is generally observed to be highest at the beginning and at the end of the growth. This is another indication that changes in the growth conditions change the probabilities of forming ZB and WZ. However, there can be a wide variety in the distribution of crystal phases and defects along the NW length, since these depend on the complicated interplay between the various growth parameters. In particular, it is difficult to obtain a perfect crystal structure throughout the whole NW because the effective V/III ratio, I_V/I_{III}, changes as the NW grows. This is seen in a typical TEM image of a self-catalysed GaAs NW (figure 11), where the temperature and beam fluxes are kept constant during growth. To explain this, we have to use dynamics.

As proposed by Ramdani *et al* [23], secondary adsorption is to a good approximation proportional to the beam flux of the material in excess (i.e. As), and such contributions are

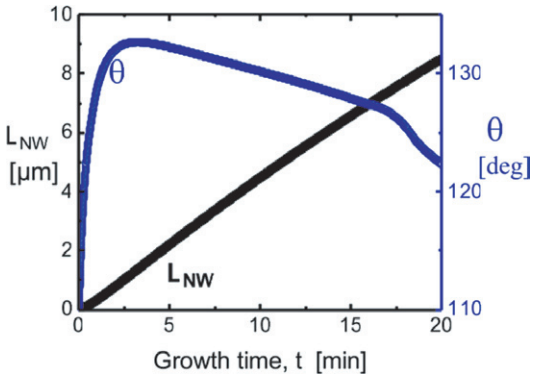

Figure 12. A typical evolution of NW growth rate and contact angle during a complete self-catalysed GaAs NW growth simulation. The initial contact angle is $\theta_{initial} = 110°$ and the NW diameter 100 nm. Main growth parameters are: $f_{As_2}/f_{Ga} = 20$, $GR_{planar} = 0.3\ \mu m\ h^{-1}$ and $T = 630\ °C$.

simply taken account of by assuming that the beam impinges on the total liquid surface. This gives effectively a higher collection from the gas states than if we only had considered direct impingement from the beam states. In these simulations, the NW diameter typically stays constant because the contact angle stays between the wetting angles on the topfacet and sidefacet, but the evolution of the liquid size is not monotonous. Relating the typical structural distribution seen in figure 11 to the typical evolution of relative size of the liquid predicted from the simulations (shown in figure 12), shows good agreement with theoretical predictions by Krogstrup *et al* [25] using the flat topfacet assumption (regime I).

The crystal structure with the highest formation probability depends on the size of the liquid phase relative to the growth interface area. This match apparently well with the present simulations, which are done in regime I. However, it should be noted that whether the overall modelling it is done in regime I or II, the evolution of the droplet size seems to be qualitatively the same. As will be seen for regime II modelling

in the next sections, truncation edge nucleation might also favour WZ at relative small droplets.

3.4. Growth of self-catalysed GaAs NWs on patterned Si(1 1 1)/SiO_x substrates

As shown by Bauer *et al* [80] and Plissard *et al* [81] it is possible grow positioned self-catalysed GaAs NW arrays using a Si/SiO_x template, and when growing the wires using a hole array in a SiO_x layer thermally grown on the Si substrate, approximately the same growth temperatures as above is used, but the Ga flux needs to be equivalent to a planar growth rate of 0.8–1.2 μm h^{-1} and the V/III flux ratios need to be in the range 1–5 (see [83, 17] for details). This is a much higher Ga flux than for growth on untreated substrates with native oxide and is an indication that the av transition rate from the thick thermally grown oxide layer is dominant for the adatom state, as also seen in. Thus, for growth on a patterned oxide layer of approx. 20–30 nm of SiO_x, the diffusion length is strongly limited by desorption for both Ga and As species. As it has not been possible to find activation enthalpies for av transitions on oxide surfaces in the literature, we simply take it to be half the value on a corresponding crystalline surface. The density of incorporation sites at the oxide surface is set to zero. For the growths on Si (1 1 1) wafers with both the native oxide layer and the thermal oxide layer, it is assumed that the low energy pathway of diffusion is one dimensional on the NW sidefacets (along the NW growth axis) and isotropic on the substrate. (See figure 13 for experimental and theoretical results on a sharp upper temperature limit for this type of growth.)

3.5. Liquid–solid growth dynamics—The single slice construction

As mentioned in sections 2.2 and 2.3, and as indicated by many recent experiments [40–42], the assumption of a perfect flat liquid–solid interface is in most cases not a good assumption when analysing the details of the liquid–solid dynamics and structural formation probabilities. To analyse the liquid–solid dynamics at the growth region in more detail we need to define a more complete parameter set $\{X\}$. To do this, we first write the Gibbs free energy of the total ls NW growth system in the form,

$$G_{\mathrm{sys},j} = \int_0^{180^\circ} \Delta G_{\mathrm{sys},j}(\omega)\,\mathrm{d}\omega, \qquad (28)$$

where $\Delta G_{\mathrm{sys},j}(\omega)$ is the free energy of a representative thin 'double cake piece' throughout the whole ls system, as shown in the top view illustration of a NW with a typical six-fold axial symmetry in figure 14(*a*).

The construction of the ls growth system at a given ω considered in this section is sketched in (*b*). For a single faceted solid crystal the equilibrium shape (called the 'Wulff shape') and can be calculated exactly if the surface energy function in equation (20) is known [82]. But the equilibrium shape of a liquid–solid system is extremely complex to derive and we will make simplifying assumptions in order to make qualitative predictions of a corresponding liquid–solid 'Wulff shape'. In section A.7 in the appendix we discuss the complete three-dimensional ls system of constant liquid curvature and complete facetting.

In equation (28), the integration over ω using analytical equations is difficult to carry out, thus we will start by

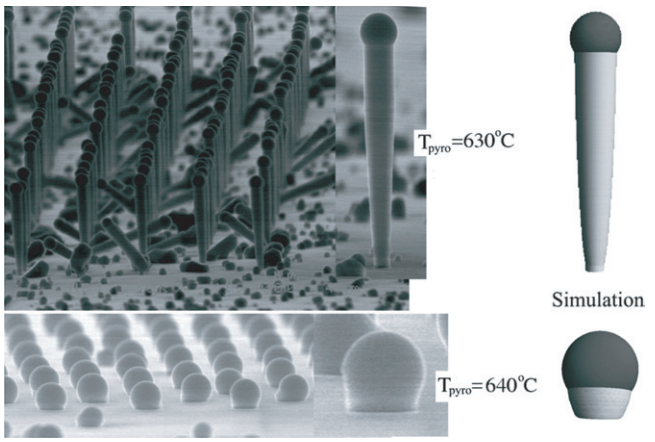

Figure 13. Investigation of the upper growth temperature limit at a given V/III ratio for positioned self-catalysed GaAs NW growth on a Si 1 1 1 substrate with a 30 nm thick SiO_x layer. The preparation of the holes in the oxide layer is done with e-beam lithography on the same 2″ wafer and all processing was carried out before the wafer was cut into four $\frac{1}{4}''$ wafers just before loading into the buffer chamber. This ensures that differences due to preprocessing steps have a minimal effect on the final results when comparing the growths. The two growths are grown under exactly same conditions for 20 min, a Ga flux corresponding to a planar GaAs growth rate of $\mathrm{GR}_{\mathrm{planar}} = 0.9\,\mu\mathrm{m\,h}^{-1}$ and a measured flux ratio of $f_{\mathrm{As}_2}/f_{\mathrm{Ga}} = 3$ (measured with an ion-gauge filament), but with two different temperatures that were measured just before initiation of the growth with a pyrometer as $T_{\mathrm{pyro}} = 630\,^\circ\mathrm{C}$ and $T_{\mathrm{pyro}} = 640\,^\circ\mathrm{C}$. The activation enthalpy for the *av* transition of Ga adatoms on the oxide is set to half the value of the modelling on native oxide and the As species was set to desorb immediately from the oxide (i.e. $\Gamma_{\mathrm{al,As}} = 0$). Using the same basic conditions in the simulations (shown on the right) the sharp temperature transition occurred at $T_{\mathrm{simulation}} = 661\,^\circ\mathrm{C}$ and $T_{\mathrm{simulation}} = 667\,^\circ\mathrm{C}$, which just means that there is still some fine tuning of parameters left to be done. The NW crystal formation completely stopped at $T_{\mathrm{simulation}} = 669\,^\circ\mathrm{C}$.

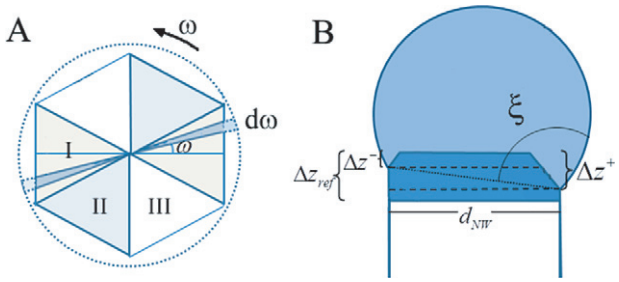

Figure 14. (*a*) Top view illustration of the liquid–solid growth region where three sections indicated with a colour and roman numerals are identical but rotated 60° degrees, both in case of ZB and WZ structure. $\Delta G_{\mathrm{sys},j}(\omega)$ is the Gibbs free energy of a single slice throughout the growth region. (*b*) Side view illustration of a suggested growth system at a given ω. The coloured region indicates the growth system (dark blue: solid, light blue: liquid), where Δz_{ref} is a reference length to a position from where the solid is considered to be fixed as measured from the topfacet. Δz_+ and Δz_- are the truncation heights at $\omega = 0°$ and $\omega = 30°$, respectively. ξ is the contact angle of the constant curvature construction and is a function of ω.

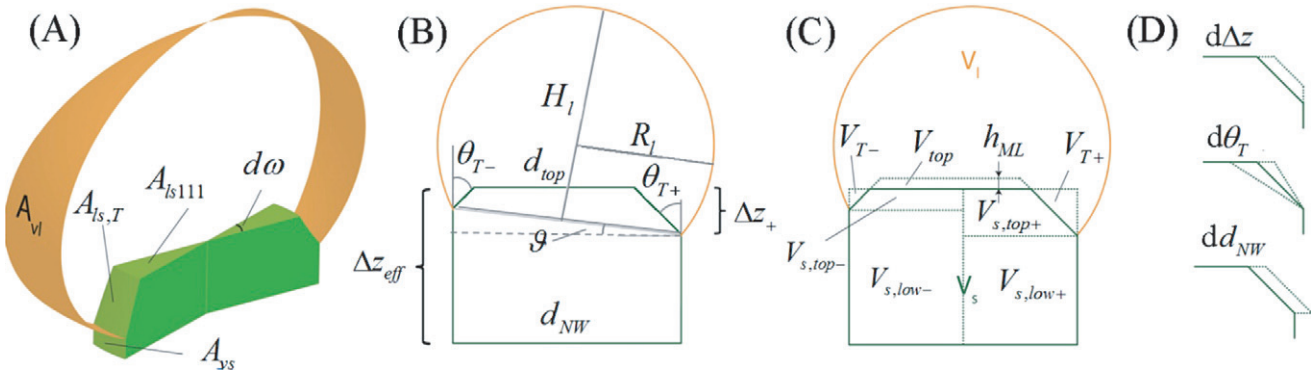

Figure 15. Single slice construction in regime II. (*a*) 3D figure showing the NW growth system used in the single slice model. (*b*) 2D illustration of the involved trigonometric quantities and (*c*) the volume elements. (*d*) 2D illustration of the three different ways the truncation can change during growth. The Gibbs free energy of this construction can be calculated using basic trigonometric relations, see section A.4 in the appendix.

looking at a single slice construction for which the liquid curvature stays constant. The choice of the parameter set $\{X(\omega)\}$ used with equation (6) when describing the dynamics of the NW growth system is obviously crucial for the overall evolution of the structure and morphology in the simulation. Recent *in situ* growth experiments have suggested that a truncated morphology at the growth interface edge is a general phenomenon, and it will therefore be taken into account here. Thus, we will choose, $\{X\} \in \{d_{\mathrm{NW}}, \Delta z_+, \Delta z_-, \theta_{\mathrm{T}+}, \theta_{\mathrm{T}-}, \xi\}$ as our parameter set (see figure 15), where $\theta_{\mathrm{T}+}$ and $\theta_{\mathrm{T}-}$ are the truncation angles at $\omega = 0^\circ$ and $\omega = 180^\circ$ respectively. Note that all these parameters are functions of , but only considering a single cut of a finite thickness (of say $\mathrm{d}\omega = 1^\circ$) can give us an idea of the mean properties of the total three-dimensional growth region. The Gibbs free energy for a single slice, $\Delta G_{\mathrm{sys,ZB(WZ)}}(\omega = 0^\circ)\,\mathrm{d}\omega$, can be found using basic trigonometric relations (see section A.4 in the appendix).

The ls system is continuously adjusting towards $\Delta\mu^X_{\mathrm{ls}} = \delta\mu_{\mathrm{l-ERS}} - \delta\mu^X_{\mathrm{s-ERS}} = 0$ conditions, but the input of free energy from the beam fluxes, vapour and adatoms and the interplay with anisotropic solid and the nucleation limited growth on the top facet keep the system out of equilibrium. Under certain conditions, the solid can enter a regime where undesired facets are locked in because a free energy barrier has to be overcome in order to form a facet lowering the total free energy of the system. The liquid–solid driving forces of liquid $\mathrm{Ga}_{1-x}\mathrm{As}_x$ assisted GaAs NW growth is plotted as a function of truncation height Δz for a certain set of fixed parameters in using equation (6) and the single slice construction around $\omega = 0^\circ$. In figure 16(*a*) it is seen that the equilibrium value of $\Delta z_\pm$ is larger for smaller systems. For the single slice construction the equilibrium morphology will always have a negative truncation. However a non-steady-state evolution of the growth system can force the system into regime I and to get back to regime II will require nucleation of a truncated facet which requires a certain formation free energy. Figure 16(*b*) shows that, in the single slice construction, varying the truncation on one side have a small effect on the truncation on the opposite side. Figure 16(*c*) shows an important general trend, namely that truncation heights are generally smallest at smallest droplet sizes. This means that relatively small droplets has higher tendency of going into regime I than larger droplets, in accordance with [26]. In figure 16(*d*), it is seen that a strong dependence of the liquid concentration on the truncation size indicates that it is the composition which plays a dominating role on the oscillating morphology.

Figures 16(*e*) and (*f*) show the driving forces around certain facets in the case of ZB and WZ structure, respectively. It is seen that for certain sets of orientations and parameters, the system needs to form another facet orientation to reach a quasi-equilibrium state. If the potential barrier to form such a facet is large, the system can enter an unstable growth mode.

In figures 17(*b*) and (*c*) it is shown that the truncation angles affect the driving forces in a more complicated way than the other parameters which are considered here. This implies that the liquid–solid growth region can stay in a dynamical metastable and still steady-state regime (see section A.5 in the appendix).

The surface energies and the interface energy function given by equation (20) play a crucial role on the NW growth simulations in general and on the truncation dynamics in particular. The interface energy function is plotted for the single slice construction in figure 17(*a*). w_{hkl}, which specifies the half-width half maximum of the energy decreases around the $(h\,k\,l)$ facet is an important parameter for the dynamical system. If w_{hkl} is small, the corresponding truncation facet orientation is locked to a low energy facet orientation and it is unlikely that the facet can overcome the energy barrier $\Delta G^{\theta_{\mathrm{T1}}-\theta_{\mathrm{T2}}}_{\mathrm{ls,III-V}}$ needed to form another facet and a more preferable configuration. In figures 17(*b*) and (*c*) shows how the ls driving force for truncation angle (i.e. the free energy change per pair due to a change in θ_{T}) depends on the orientation for a given parameter set, where $\Delta z = 2\,\mathrm{nm}$ is closer to equilibrium than $\Delta z = 1\,\mathrm{nm}$. We emphasize that in this continuum approach with single truncation facets it has not been taken into account that facet orientations becomes discrete when Δz becomes small. The formation of a new facet orientation can be nucleation limited if the barrier is larger than the single transition state barrier $\Delta G^{\theta_{\mathrm{T1}}-\theta_{\mathrm{T2}}}_{\mathrm{ls,III-V}} > \delta g^{\mathrm{TS,ERS}}_{\mathrm{ls,III-V}}$ and such a transition has to be treated in a framework similar

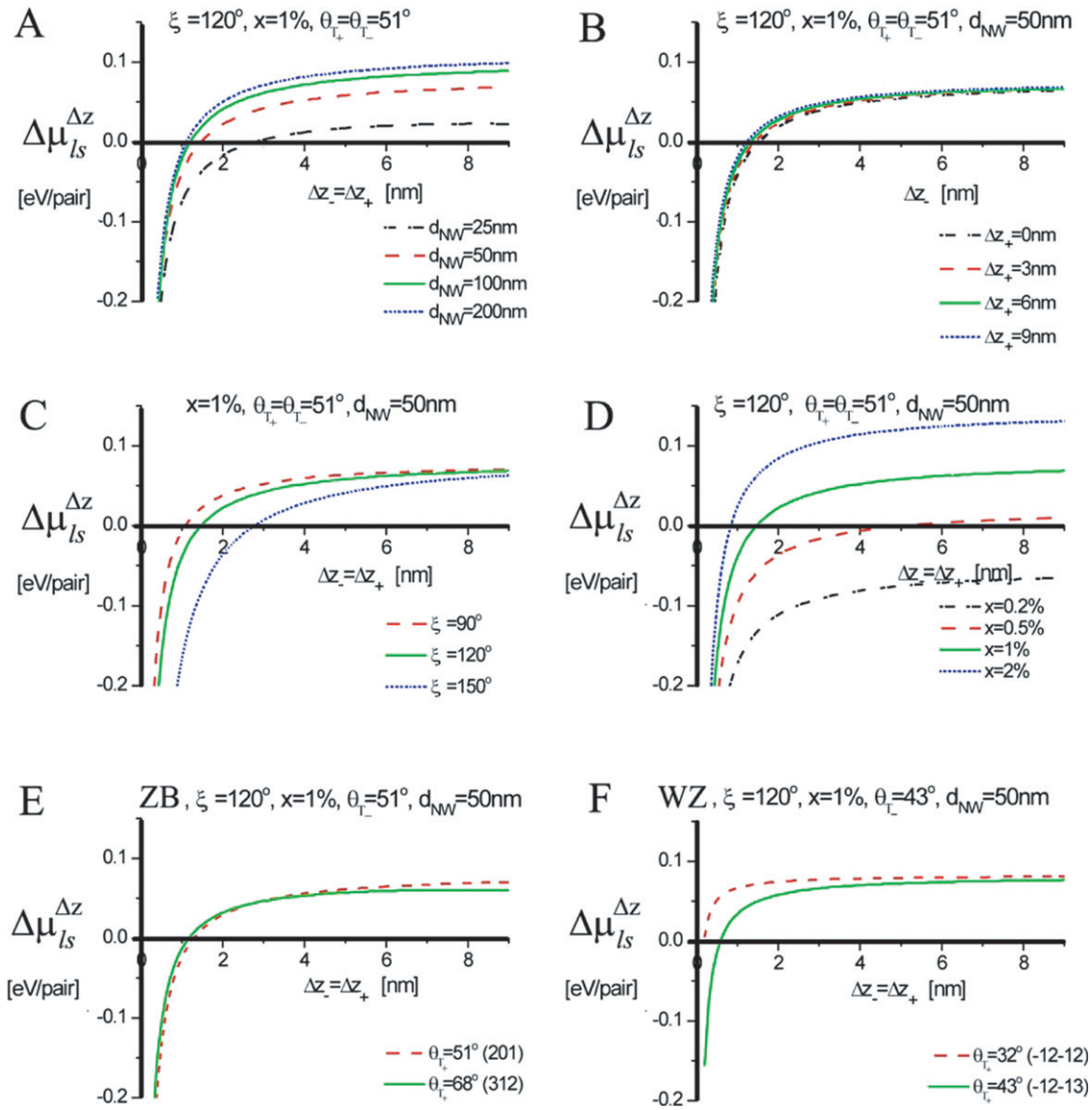

Figure 16. Plots of driving forces $\Delta\mu^{\Delta z}_{\mathrm{ls,III-V}} = \delta\mu_{\mathrm{l-ERS.III-V}} - \delta\mu^{\Delta z}_{\mathrm{s-ERS.III-V}}$ of Ga Assisted GaAs NW growth as a function of the truncation size for the single slice construction at $\omega = 0^\circ$ with $\{1\,\bar{1}\,0\}$ type sidefacets at $T = 630\,^\circ$C. The equilibrium value of the parameters under the chosen growth conditions are where $\Delta\mu_{\mathrm{ls}} = 0$. (*a*) The equilibrium value of $\Delta z_\pm$ is larger for smaller systems. For the single slice construction the equilibrium morphology will always have a negative truncation. (*b*) By varying the truncation on one side has a small effect on the truncation on the opposite side in the single slice construction. (*c*) Truncation heights are generally smallest at smallest droplet sizes. (*d*) A strong dependence of the liquid concentration on the truncation size indicates that it is the composition which plays a dominating role on the oscillating morphology. (*e*) and (*f*) shows the driving forces around certain facets in the case of ZB and WZ structures, respectively.

to that of section 2.3. However these transitions will not be treated in detail here; instead, in the simulations the probability of forming another truncation facet orientation simply depends on the evolution of the system morphology. For large values of $w_{h\,k\,l}$ the angle of the truncation facet can change more or less freely and it will oscillate in accordance with the oscillations of the growth system. However, to make qualitative predictions about a given growth process and the structural formation probabilities it is necessary to have reasonably good estimates of the parameters describing the surface energy functions. This is indicated in figure 18 where each set of simulation parameters gives different results.

For the single slice construction, it is possible to predict the impact of the growth interface size and morphology on the relative formation rates of the ZB and WZ stacking's, given a set of simulation parameters. In figures 18(*a*), (*b*), (*c*) three different simulations S1, S2, S3 of the truncation dynamics show some general trends as a function of the growth interface diameter, even though huge quantitative differences are seen due to changes in the parameters determining the shape of the interface energy functions. The quantities which are plotted here are average values after reaching a quasi-steady state; see section A.5 in the appendix for examples of the truncation dynamics. Parameters used for the simulations are listed in section A.3 in the appendix. If truncation edge nucleation dominates at the topfacet, WZ would be favoured at small diameters and ZB at larger diameters (figure 18(*a*)) if considering the interface energy function as plotted in.

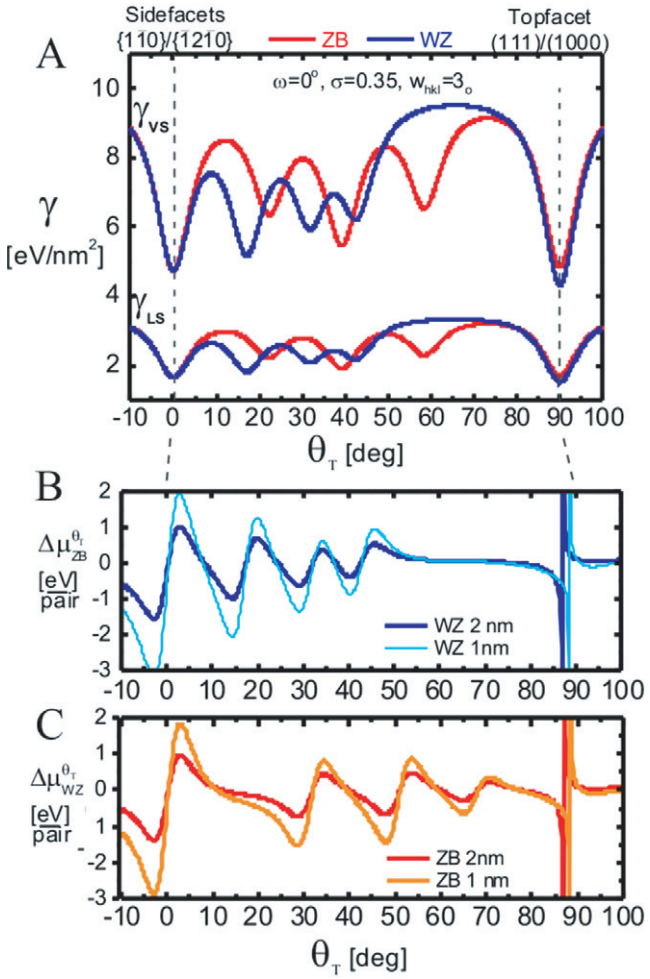

Figure 17. (*a*) The 2D γ-plots using equation (20) for the vs and ls interfaces around $\omega = 0^\circ$ and $\gamma_{pq0} = 10\,\mathrm{eV\,nm^{-2}}$. It is seen that WZ is dominant at small truncation angles θ_T and ZB is dominant at large θ_T. (*b*), (*c*) Driving forces $\Delta\mu^{\theta_\mathrm{T}}_{\mathrm{ls},i} = \delta\mu_{\mathrm{l-ERS},i} - \delta\mu^{\theta_\mathrm{T}}_{\mathrm{s-ERS},i}$ of ZB and WZ is plotted as a function truncation facet angle for ZB and WZ, respectively. The parameter set are $d_\mathrm{NW} = 50\,\mathrm{nm}$, $\xi = 120^\circ$, $x_\mathrm{V} = 1\%$ and $\theta_{\mathrm{T}+} = 51^\circ$ for ZB and $\theta_{\mathrm{T}+} = 43^\circ$ for WZ. The stable points are the ones where the driving force is zero and the gradient of the driving force is positive. The plot tells us that it is not possible to switch freely between facet orientations. The singularities close to 90° is due to the definition of the truncation angle shown in figure 15(*d*), because the system cannot approach a single topfacet for a fixed Δz value (see section A.3 in the appendix for the low energy orientations used).

In figure 18(*b*) it is seen that the truncation facet seems to be smaller with increasing size of the liquid–solid growth region, even though it does not necessarily have a monotonic dependence due to the anisotropic interface energy. In figure 18(*c*) it is shown that the axial growth rate is strongly dependent on the size of the growth region. However, the actual dependence is not simple depends on the simulation parameters used, where the relative liquid size does also play an important role on the truncation angle as seen in figure 18(*d*). Thus, because values for the surface energy function, the various energy barriers and kinetic reaction constants are not well known, the modelling of NW growth is still far from being a supplement to NW growth experiments.

4. Summary

We have presented a detailed review on and overall treatment of the theoretical formalism of III–V NW growth dynamics, using the current understanding of NW growth. The overall treatment can be used analyse and model the dynamics of axial III–V NW growth via the vapour–liquid–solid mechanism as a function of the basic growth parameters, partial pressures/beam fluxes and substrate temperature. The formalism relies on transition state kinetics driven by minimization of free energy of the total system. All chemical potentials are measured with respect to a common equilibrium reference state where the total system is in a thermodynamical equilibrium. The formalism makes it possible to understand the complex mechanisms of NW growth dynamics in greater detail and can serve as strong analysing tool when optimizing VLS growth of III–V nanowires. We have implemented the theoretical framework into a computer simulation model, and even though the program is in a preliminary stage, the modelling examples show growth good agreement with experiments and that the theory can be used to model NW growth dynamics in a new level of detail.

Acknowledgments

This work was supported by the Danish National Advanced Technology Foundation through project 022-2009-1, the Danish Strategic Research Council through project 09-065736 and the ERC starting grant ‘UpCon’.

Appendix

A.1. Adatom collection

For the condensed adatom regime, it can be shown (using mass conservation) that the general equation for steady-state adatom collection can be written in a relatively compact form,

$$\Delta\Gamma_{\mathrm{al},i} = \frac{2\pi}{l_j}\sum_{r'=\frac{d_\mathrm{NW}}{2}}^{\infty} r'(\Delta\Gamma_{(\mathrm{vb})a_{r'},i} - \Delta\Gamma_{a_{r'}\mathrm{s},i}) + \sum_{l=0}^{\frac{L_{NW}}{h_{ML}}} (\Delta\Gamma_{(\mathrm{vb})a_l,i} - \Delta\Gamma_{a_l\mathrm{s},i}), \tag{29}$$

where the first summation accounts for the net transition flux from the substrate to the sidefacets and the second summation for the net generation of adatoms from the beam and the vapour along the NW sidewalls. $a_{r'(l)}$ is the adatom site at r'(or l) along the substrate (or NW) surface as measured from the NW foot. l_j is the distance between the two adjacent adatom sites. The substrate diffusion is assumed to be isotropic, which is a reasonable for growths carried out on substrates with a (1 1 1) orientation or substrates covered with an amorphous oxide layer. A simple approach is to assume that there exist certain effective collection areas characterized by corresponding effective diffusion lengths [56]. Even though this approach is not very accurate for modelling the growth dynamics, it is instructive and intuitive. To get a

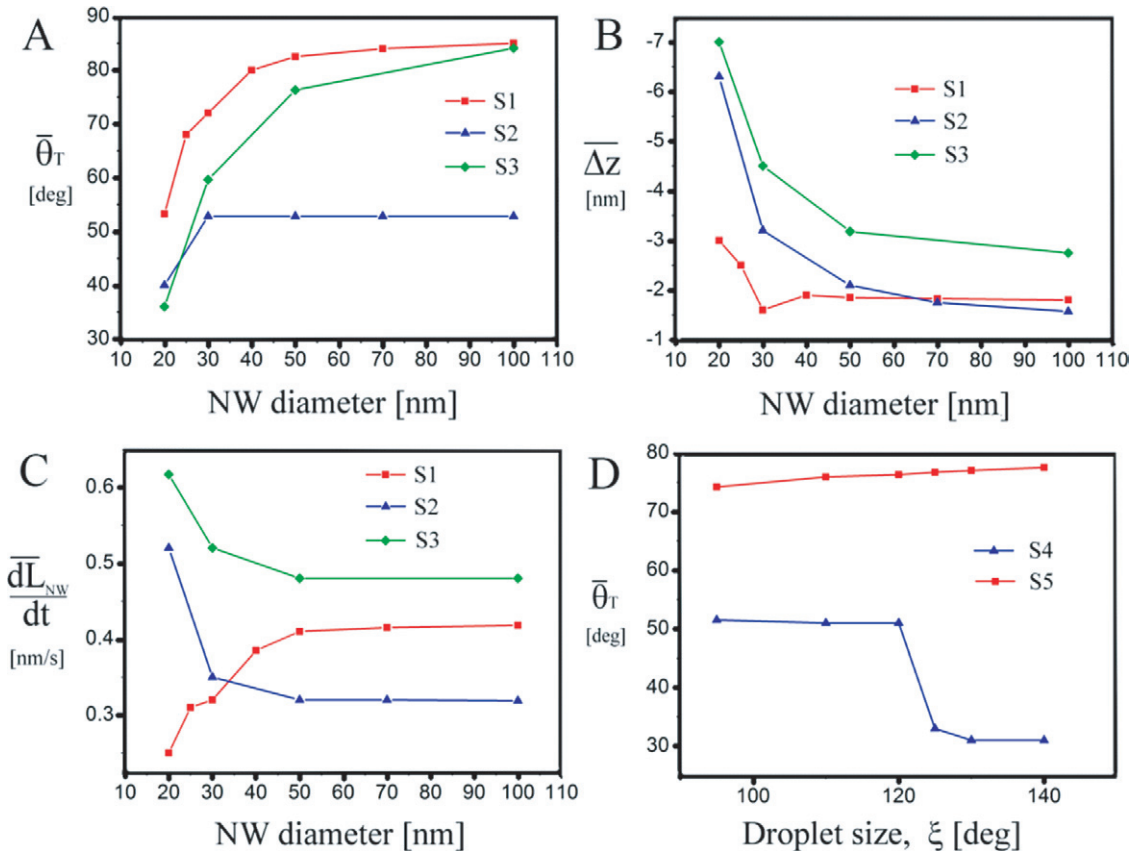

Figure 18. Average values taken from growth simulations of self-catalysed GaAs growth in the single slice construction (at $\omega = 0^\circ$ where the system choose symmetry, i.e. $\Delta z = \Delta z_- = \Delta z_+$ and $\theta_T = \theta_{T-} = \theta_{T+}$). (*a*), (*b*), (*c*) Three different simulations with parameters, S1, S2, S3 (listed in section A.3 in the appendix) of the truncation dynamics show some general trends as a function of the system size. The quantities which are plotted here are average values after reaching a quasi-steady state, see section A.5 in the appendix for examples of the truncation dynamics. See text for discussion.

more intuitive feeling of the adatom kinetics in terms of a diffusion length in the transition state approach, adatom migration on a large homogeneous planar interface serves as a good example. Then all parameters are translation invariant and there is no net diffusion. Since in this case we do not have to distinguish between the adatoms as all states are independent of position in the continuum approach we will just label all adatoms with an 'a'. There are three main transition paths for an adatom; surface diffusion (aa), desorption (av) and incorporation (as). The as mechanism can be further divided into two types of incorporation mechanisms: incorporation at a favourable site (such as a kink) leading to radial growth, or by interdiffusion which can take place at all sites. Incorporation by interdiffusion is only relevant for impurities such as dopants since exchange of group III and V element will not have a net effect on the adatom state, and will therefore be neglected here. In such conditions, an adatom diffusion length is a well-defined quantity. The mean length displacement (i.e. the mean distance between the location of 'birth' and 'death' events, where 'death' is determined by either an 'as′ or 'av′ transition) is $\lambda_{j,i} = \sqrt{D_{j,i}\tau_{j,i}}$, where $D_{j,i} = Z_{\mathrm{aa},i}\upsilon_{\mathrm{a},i}l_j^2(1-\bar{\rho}_{j,i})\exp(-((\delta g_{\mathrm{aa},i}^{\mathrm{TS,ERS}} - \delta\mu_{\mathrm{a-ERS},i})/k_\mathrm{B}T))$, is the mean adatom diffusivity, and $\tau_{j,i} = (\tau_{j,i,\mathrm{as}}^{-1}+\tau_{j,i,\mathrm{av}}^{-1})^{-1}$ is the average adatom lifetime. Here l_j is the distance between the two adjacent adatom sites along the lowest energy direction(s), with activation free energy $\delta g_{\mathrm{aa},i}^{\mathrm{TS}}$. For simplicity, higher energy directions are ignored. If an adatom occupies a given site, it is impossible for another adatom to jump into the same site. Thus, the concentration of free sites, $1-\bar{\rho}_{j,i}$, is included in the diffusivity, $\bar{\rho}_{j,i}$ being the normalized adatom density. The lifetimes ended by an 'as′ or 'av′ state transition are inversely proportional to the respective transition rates,

$$\tau_{j,i,\mathrm{as}} = \frac{1}{\bar{Z}_{\mathrm{as},i}\bar{c}_{\mathrm{inc},i}\upsilon_{\mathrm{a},i}}\exp\left(\frac{\delta g_{\mathrm{as},i}^{\mathrm{TS,ERS}} - \delta\mu_{\mathrm{a-ERS},i}}{k_\mathrm{B}T}\right)$$

and

$$\tau_{j,i,\mathrm{av}} = \frac{1}{\bar{Z}_{\mathrm{av},i}\upsilon_{\mathrm{a},i}}\exp\left(\frac{\delta g_{\mathrm{av},i}^{\mathrm{TS,ERS}} - \delta\mu_{\mathrm{a-ERS},i}}{k_\mathrm{B}T}\right),$$

respectively. $\bar{c}_{\mathrm{inc},i}$ is the normalized density of probable incorporation sites (kinks or possibly steps at high adatom densities and/or low temperatures). This important factor illustrates a major difference between the av and as transitions, namely that desorption can take place everywhere, which is not the case for incorporation. $\tau_{j,i,\mathrm{as}}$ is conditioned by the incorporation of both a group III and a group V element because of the fixed 1 : 1 stoichiometry of the III–V solid. For the

modelling, $\tau_{j,i,\mathrm{as}}$ is limited by incorporation of an adatom at a kink site, which means that the solid chemical potential equals the ERS potential, and possible sidefacet nucleation events will not be considered. For desorption of adatoms, the intrinsic activation barrier[8] $\delta g_{\mathrm{av},i}^{\mathrm{TS,ERS}}$ is independent of the other components.

The general equation for the adatom diffusion length at a given point at a homogeneous interface is therefore:

$$\lambda_{j,i} = \left[\bar{Z}_{\mathrm{aa},i} l_{\mathrm{a},i}^2 (1-\bar{\rho}_{j,i}) \exp\left(-\frac{\delta g_{\mathrm{aa},i}^{\mathrm{TS,ERS}}}{k_{\mathrm{B}}T}\right) \times \left(\bar{Z}_{\mathrm{as},i} \bar{c}_{\mathrm{inc},i} \exp\left(-\frac{\delta g_{\mathrm{as},i}^{\mathrm{TS,ERS}}}{k_{\mathrm{B}}T}\right) + \bar{Z}_{\mathrm{av},i} \exp\left(-\frac{\delta g_{\mathrm{av},i}^{\mathrm{TS,ERS}}}{k_{\mathrm{B}}T}\right)\right)^{-1} \right]^{1/2}, \quad (30)$$

which is apparently independent of chemical potential and vibration frequency of the adatoms. However the number of incorporation sites $\bar{c}_{\mathrm{inc},i}$ depends on the local adatom densities of both components and on the orientation of the local facet, and is therefore also dependent on the chemical potential of the local adatom state, see equation (4).

A.2. Adatom transition state diffusion calculations using an uniform 'Dubrovskii/Johansson' diffusion scheme

Calculating the adatom density distribution using the general adatom diffusion equation, equation (29), in terms of growth conditions has proved to be difficult. Here we will show a simplified approach by using the transition state fluxes in a classical Fickian diffusion scheme to find the adatom density distribution in terms of the basic growth parameters. As in previous studies [83, 17] we only distinguish between two types of facets, the NW sidefacets (NW) and a planar substrate facet (*sub*). If we for simplicity assume that; $1-\bar{\rho}_{j,i} \approx 1$, and that $\bar{c}_{\mathrm{inc},i}$ is a constant along the length, meaning that the diffusion length only varies with time and does not vary along a given facet. Thus two coupled diffusion equations,

$$D_{\mathrm{NW},i} \frac{\mathrm{d}^2}{\mathrm{d}z^2} \rho_{\mathrm{NW},i}(z) = D_{\mathrm{NW},i} \frac{\rho_{\mathrm{NW},i}(z)}{\lambda_{\mathrm{NW},i}^2} - f_{\mathrm{NW},i,\perp} - \Gamma_{\mathrm{sa(NW)},i} - \Gamma_{\mathrm{va(NW)},i}$$

and

$$D_{\mathrm{sub},i} \frac{1}{r} \frac{\mathrm{d}}{\mathrm{d}r} \left(r \frac{\mathrm{d}}{\mathrm{d}r} \rho_{\mathrm{sub},i}(r) \right) = D_{\mathrm{sub},i} \frac{\rho_{\mathrm{sub},i}(r)}{\lambda_{\mathrm{sub},i}^2} - f_{\mathrm{sub},i,\perp} - \Gamma_{\mathrm{sa(sub)},i} - \Gamma_{\mathrm{va(NW)},i}$$

need to be solved. Here the diffusivity will be assumed uniform, $D_{j,i} = Z'_{\mathrm{aa},i} \upsilon_{\mathrm{a},i} l_j^2 \exp(-(\delta h_{\mathrm{aa},i}^{\mathrm{TS,ERS}}/k_{\mathrm{B}}T))$. If shadowing effects and influence from other NWs on the substrate are ignored we can assume that $\mathrm{d}\rho_{\mathrm{sub},i}/\mathrm{d}r|_{r\to\infty} = 0$. The average incoming beam fluxes are given as $f_{\mathrm{NW},i,\perp} = f_i \sin(\varphi_i)/\pi$ and $f_{\mathrm{sub},i,\perp} = f_i \cos(\varphi_i)$, where φ_i is the angle of the incoming beam of group i with respect to the substrate normal. $1/\pi$ is the fraction of the NW facets which is exposed to the beam which is perfectly consistent with the transition state approach where transitions are independent of the state they are moving into. Solutions are then of the form,

$$\rho_{\mathrm{NW},i}(z) = C_1 \exp\left(\frac{z}{\lambda_{\mathrm{NW},i}}\right) + C_2 \exp\left(-\frac{z}{\lambda_{\mathrm{NW},i}}\right) + \frac{\lambda_{\mathrm{NW},i}^2 \left(\frac{f_i \sin(\varphi_i)}{\pi} + \Gamma_{\mathrm{sa},i} + \sum_n \Gamma_{\mathrm{va},i_n} \right)}{D_{\mathrm{NW},i}}, \quad (31)$$

$$\rho_{\mathrm{sub},i}(z) = C_3 K_{0,\frac{r}{\lambda_{\mathrm{NW},i}}} + \frac{\lambda_{\mathrm{sub},i}^2 \left(f_i \cos(\varphi_i) + \Gamma_{\mathrm{sa},i} + \sum_n \Gamma_{\mathrm{va},i_n} \right)}{D_{\mathrm{sub},i}}, \quad (32)$$

where $K_{h,x}$ is the modified Bessel function of order h evaluated at x. To solve for the constants (C_i) we need three boundary conditions;

$$D_{\mathrm{NW},i} \left. \frac{\mathrm{d}\rho_{\mathrm{NW},i}}{\mathrm{d}z} \right|_{z=L_{\mathrm{NW}}} = \Delta\Gamma_{\mathrm{al},i}, \quad (33)$$

$$D_{\mathrm{NW},i} \left. \frac{\mathrm{d}\rho_{\mathrm{NW},i}}{\mathrm{d}z} \right|_{z=0} = -D_{\mathrm{sub},i} \left. \frac{\mathrm{d}\rho_{\mathrm{sub},i}}{\mathrm{d}r} \right|_{r=\frac{d_{\mathrm{NW}}}{2}}, \quad (34)$$

$$\rho_{\mathrm{NW},i}(z=0) = \rho_{\mathrm{sub},i}\left(r = \frac{d_{\mathrm{NW}}(z=0)}{2}\right). \quad (35)$$

Equation (33) assumes quasi-steady-state growth, combining the adatom to adatom state transition flux at $z = L_{\mathrm{NW}}$ with the net adatom to liquid state transition flux, which is driven primarily by the thermodynamic driving force. Because the $\Delta\Gamma_{\mathrm{al},i}$ depends on the adatom density, $\rho_{\mathrm{NW},i}(L_{\mathrm{NW}}, \delta\mu_{\mathrm{a-ERS},i})$, it needs to be isolated in equation (31) before it is put into equation (4). Using equation (7) for $\Gamma_{\mathrm{sa},i}$ and $\Gamma_{\mathrm{va},i}$, with $c_{\mathrm{v},i} = p_i/RT$ (the ideal gas law), $\delta\mu_{\mathrm{a-ERS},i}$ (which depends on the adatom densities) is solved numerically at every time step and before being put back into $\Delta\Gamma_{\mathrm{al},i}$. Equation (34) combines the adatom fluxes at the NW root, whereas equation (35) assumes a continuous adatom density function across the substrate–nanowire interface, see [86, 87]. Equation (35) requires that the transition state barriers across the NW–substrate interface are symmetric.

Solving the coupled adatom diffusion equations for diffusion along the NW facets and on an isotropic substrate with the boundary conditions, equation (33)–(35), leads to the following expression for the adatom density on the NW

[8] In this continuum approach, these activation free energies should be seen as effective values depending on the surface reconstruction and the roughness of the facet, and is in principle also temperature dependent. However for a given surface reconstruction, surface roughness and therefore $\Delta g_{sa,i}$ is a slowly varying function of T and can reasonably be ignored within the typical growth temperature range of a given type of III–V NW growth.

sidewall,

$$\rho_{\mathrm{NW},i}(z) = \frac{\lambda_{\mathrm{NW},i}}{D_{\mathrm{NW},i}} \left[\begin{pmatrix} -\cosh\left(\frac{z}{\lambda_{\mathrm{NW},i}}\right) K_{0,\frac{d_{\mathrm{NW}}}{2\lambda_{\mathrm{sub},i}}} D_{\mathrm{NW},i}\lambda_{\mathrm{sub},i}\Delta\Gamma_{\mathrm{al},i} \\ +\cosh\left(\frac{z-L_{\mathrm{NW}}}{\lambda_{\mathrm{NW},i}}\right) K_{1,\frac{d_{\mathrm{NW}}}{2\lambda_{\mathrm{sub},i}}} (\Gamma_{\mathrm{sub},i} D_{\mathrm{NW},i}\lambda^2_{\mathrm{sub},i} \\ -\Gamma_{\mathrm{NW},i} D_{\mathrm{sub},i}\lambda^2_{\mathrm{NW},i}) - \sinh\left(\frac{z}{\lambda_{\mathrm{NW},i}}\right) K_{1,\frac{d_{\mathrm{NW}}}{2\lambda_{\mathrm{sub},i}}} \\ \times D_{\mathrm{sub},i}\lambda_{\mathrm{NW},i}\Delta\Gamma_{\mathrm{al},i} + \cosh\left(\frac{L_{\mathrm{NW}}}{\lambda_{\mathrm{NW},i}}\right) K_{1,\frac{d_{\mathrm{NW}}}{2\lambda_{\mathrm{sub},i}}} \\ \times \Gamma_{\mathrm{NW},i} D_{\mathrm{sub},i}\lambda^2_{\mathrm{NW},i} + \sinh\left(\frac{L_{\mathrm{NW}}}{\lambda_{\mathrm{NW},i}}\right) K_{0,\frac{d_{\mathrm{NW}}}{2\lambda_{\mathrm{sub},i}}} \\ \times \Gamma_{\mathrm{NW},i}\lambda_{\mathrm{sub},i}\lambda_{\mathrm{NW},i} \end{pmatrix} \right] \times \left[\begin{matrix} \cosh\left(\frac{L_{\mathrm{NW}}}{\lambda_{\mathrm{NW},i}}\right) K_{1,\frac{d_{\mathrm{NW}}}{2\lambda_{\mathrm{sub},i}}} D_{\mathrm{sub},i}\lambda_{\mathrm{NW},i} \\ +\sinh\left(\frac{L_{\mathrm{NW}}}{\lambda_{\mathrm{NW},i}}\right) K_{0,\frac{d_{\mathrm{NW}}}{2\lambda_{\mathrm{sub},i}}} D_{\mathrm{NW},i}\lambda_{\mathrm{sub},i} \end{matrix} \right]^{-1}, \tag{36}$$

where $\Gamma_{j,i} = f_{j,i,\perp} + \Gamma_{\mathrm{va},i} + \Gamma_{\mathrm{sa},i}$ is the generation flux of i adatoms of the j'th surface. As $\Delta\Gamma_{\mathrm{al},i}$ is a function of $\rho_{\mathrm{NW},i}(z = L_{\mathrm{NW}})$, $\rho_{\mathrm{NW},i}$ is isolated in equation (36), without isolating $\rho_{\mathrm{NW},i}$ from $\delta\mu_{\mathrm{a-ERS},i}$ we get,

$$\rho_{\mathrm{NW},i}(L_{\mathrm{NW}}) = \left[\begin{pmatrix} \cosh\left(\frac{L_{\mathrm{NW}}}{\lambda_{\mathrm{NW},i}}\right) K_{0,\frac{d_{\mathrm{NW}}}{2\lambda_{\mathrm{sub},i}}} D_{\mathrm{NW},i}\lambda_{\mathrm{sub},i}\,\Xi_{\mathrm{al},i} \\ \times \exp\left(-\frac{\Delta g^{\mathrm{ERS}}_{\mathrm{al},i} - \delta\mu_{\mathrm{1-ERS},i}}{k_{\mathrm{B}}T}\right) \frac{\bar{\rho}^{\mathrm{ERS}}_i}{x^{\mathrm{ERS}}_i} x_i \\ + K_{1,\frac{d_{\mathrm{NW}}}{2\lambda_{\mathrm{sub},i}}} (\Gamma_{\mathrm{sub},i} D_{\mathrm{NW},i}\lambda^2_{\mathrm{sub},i} \\ -\Gamma_{\mathrm{NW},i} D_{\mathrm{sub},i}\lambda^2_{\mathrm{NW},i}) \\ - \sinh\left(\frac{L_{\mathrm{NW}}}{\lambda_{\mathrm{NW},i}}\right) K_{1,\frac{d_{\mathrm{NW}}}{2\lambda_{\mathrm{sub},i}}} D_{\mathrm{sub},i}\lambda_{\mathrm{NW},i}\,\Xi_{\mathrm{al},i} \\ \times \exp\left(-\frac{\Delta g^{\mathrm{ERS}}_{\mathrm{al},i} - \delta\mu_{\mathrm{1-ERS},i}}{k_{\mathrm{B}}T}\right) \frac{\bar{\rho}^{\mathrm{ERS}}_i}{x^{\mathrm{ERS}}_i} x_i \\ + \cosh\left(\frac{L_{\mathrm{NW}}}{\lambda_{\mathrm{NW},i}}\right) K_{1,\frac{d_{\mathrm{NW}}}{2\lambda_{\mathrm{sub},i}}} \Gamma_{\mathrm{NW},i} D_{\mathrm{sub},i}\lambda^2_{\mathrm{NW},i} \\ + \sinh\left(\frac{L_{\mathrm{NW}}}{\lambda_{\mathrm{NW},i}}\right) K_{0,\frac{d_{\mathrm{NW}}}{2\lambda_{\mathrm{sub},i}}} \Gamma_{\mathrm{NW},i}\lambda_{\mathrm{sub},i}\lambda_{\mathrm{NW},i} \end{pmatrix} \right] \times \left[\begin{pmatrix} \frac{D_{\mathrm{NW},i}}{\lambda_{\mathrm{NW},i}} \left(\cosh\left(\frac{L_{\mathrm{NW}}}{\lambda_{\mathrm{NW},i}}\right) K_{1,\frac{d_{\mathrm{NW}}}{2\lambda_{\mathrm{sub},i}}} D_{\mathrm{sub},i}\lambda_{\mathrm{NW},i} \right. \\ \left. + \sinh\left(\frac{L_{\mathrm{NW}}}{\lambda_{\mathrm{NW},i}}\right) K_{0,\frac{d_{\mathrm{NW}}}{2\lambda_{\mathrm{sub},i}}} D_{\mathrm{NW},i}\lambda_{\mathrm{sub},i} \right) \\ + \frac{1}{\rho}\cosh\left(\frac{L_{\mathrm{NW}}}{\lambda_{\mathrm{NW},i}}\right) K_{0,\frac{d_{\mathrm{NW}}}{2\lambda_{\mathrm{sub},i}}} D_{\mathrm{NW},i}\lambda_{\mathrm{sub},i}\,\Xi_{\mathrm{al},i} \\ \times \exp\left(-\frac{\Delta g^{\mathrm{ERS}}_{\mathrm{al},i} - \delta\mu_{\mathrm{a-ERS},i}}{k_{\mathrm{B}}T}\right) \\ -\frac{1}{\rho}\sinh\left(\frac{L_{\mathrm{NW}}}{\lambda_{\mathrm{NW},i}}\right) K_{1,\frac{d_{\mathrm{NW}}}{2\lambda_{\mathrm{sub},i}}} D_{\mathrm{sub},i}\lambda_{\mathrm{NW},i}\,\Xi_{\mathrm{al},i} \\ \times \exp\left(-\frac{\Delta g^{\mathrm{ERS}}_{\mathrm{al},i} - \delta\mu_{\mathrm{a-ERS},i}}{k_{\mathrm{B}}T}\right) \end{pmatrix} \right]^{-1}. \tag{37}$$

Note that $\Xi_{\mathrm{al},i}$ is a triple line flux, i.e. a particle transfer per length per time. If we assume a barrier free al transition, the exponentials vanish in equation (37) and the only dependence on $\delta\mu_{a_j-\mathrm{ERS,III(V)}}$ is through the diffusion lengths. $\delta\mu_{a_j-\mathrm{ERS,III(V)}}(\rho_{j,\mathrm{III}}, \rho_{j,\mathrm{V}}, T)$ at $z = L_{\mathrm{NW}}$ can now be solved numerically at every step time in a double iterative process for both $\bar{\rho}_{j,\mathrm{III}}(z = L_{\mathrm{NW}})$ and $\bar{\rho}_{j,\mathrm{V}}(z = L_{\mathrm{NW}})$ choosing certain initial values, step size and acceptable error values depending on the computation time available and accuracy needed. The principle of a single numerical computation loop in a typical math language (here Mathcad) is shown below,

$$\delta\mu_{a_j-\mathrm{ERS,III(V)}}(\rho_{\mathrm{NW},i}, T, \delta\mu_{\mathrm{quess,III}}, \delta\mu_{\mathrm{quess,V}}, \mathrm{step}, \mathrm{error})_i =$$

$$\begin{array}{l} \delta\mu_{\mathrm{III(V)}} \leftarrow \delta\mu_{\mathrm{quess,III(V)}} \\ \delta\mu_{\mathrm{V(III)}} \leftarrow \delta\mu_{\mathrm{quess,V(III)}} \\ \Delta_{\mathrm{III(V)}} \leftarrow 1\,\mathrm{eV} \\ \text{while } |\Delta_{\mathrm{III(V)}}| > \mathrm{error} \\ \quad \left| \begin{array}{l} F_{\mathrm{III}} \leftarrow \delta\mu_{a_j-\mathrm{ERS,III}}(\rho_{j,\mathrm{III}}(L_{\mathrm{NW}}, \delta\mu_{\mathrm{III}}), \\ \qquad \rho_{j,\mathrm{V}}(L_{\mathrm{NW}}, \delta\mu_{\mathrm{V}}), T) \\ F_{\mathrm{V}} \leftarrow \delta\mu_{a_j-\mathrm{ERS,V}}(\rho_{j,\mathrm{III}}(L_{\mathrm{NW}}, \delta\mu_{\mathrm{III}}), \\ \qquad \rho_{j,\mathrm{V}}(L_{\mathrm{NW}}, \delta\mu_{\mathrm{V}}), T) \\ G_{\mathrm{III}} \leftarrow \delta\mu_{\mathrm{III}} \\ G_{\mathrm{V}} \leftarrow \delta\mu_{\mathrm{V}} \\ \Delta_{\mathrm{III}} \leftarrow F_{\mathrm{III}} - G_{\mathrm{III}} \\ \Delta_{\mathrm{V}} \leftarrow F_{\mathrm{V}} - G_{\mathrm{V}} \\ \delta\mu_{\mathrm{III(V)}} \leftarrow \delta\mu_{\mathrm{III(V)}} + \mathrm{step}\cdot\mathrm{sign}(\Delta_{\mathrm{III(V)}}) \\ \qquad \text{if } |\Delta_{\mathrm{III(V)}}| > \mathrm{error} \wedge |\Delta_{\mathrm{V(III)}}| > \mathrm{error} \end{array} \right. \\ \begin{pmatrix} \delta\mu_{\mathrm{III}} \\ \delta\mu_{\mathrm{V}} \end{pmatrix} \end{array} \tag{38}$$

where $\delta\mu_{a_j-\mathrm{ERS,III(V)}}(\rho_{j,\mathrm{III}}(L_{\mathrm{NW}}, \delta\mu_{\mathrm{III}}), \rho_{j,\mathrm{V}}(L_{\mathrm{NW}}, \delta\mu_{\mathrm{V}}), T)$ is given by equation (4) with $\bar{\rho}_{j,\mathrm{III(V)}}(L_{\mathrm{NW}}, \delta\mu_{\mathrm{III(V)}})$ being the value from equation (37). The calculated value of $\delta\mu_{a_{\mathrm{NW}}-\mathrm{ERS,III(V)}}$ is a 1×2 matrix with $\delta\mu_{a_{\mathrm{NW}}-\mathrm{ERS,III}}$ and $\delta\mu_{a_{\mathrm{NW}}-\mathrm{ERS,V}}$ on each position. Note that much computation time is saved by choosing the simplest version $\delta\mu_{a_{\mathrm{NW}}-\mathrm{ERS},i}(\rho_{\mathrm{NW},i}, T) \cong k_{\mathrm{B}}T\ln(\bar{\rho}_{\mathrm{NW},i}(z = L_{\mathrm{NW}})/\bar{\rho}^{\mathrm{ERS}}_{\mathrm{NW},i})$, which only requires one iteration loop for each element at each time step, which may be a rough but fairly reasonable simplification at low total fluxes and if only looking at axial growth. After this step, $\delta\mu_{a_{\mathrm{NW}}-\mathrm{ERS},i}(\rho_{\mathrm{NW},i}, T)$, is finally put into equation (37) which is again put into equations (14) and (36).

Solving for the adatom density on the isotropic substrate (which is a reasonable approximation on (1 1 1) surfaces and amorphous oxide layers), leads to the following solution,

$$\rho_{\mathrm{sub},i}(r) = \frac{\lambda_{\mathrm{sub},i}}{D_{\mathrm{sub},i}} \left[\begin{pmatrix} \cosh\left(\frac{L_{\mathrm{NW}}}{\lambda_{\mathrm{NW},i}}\right) K_{1,\frac{d_{\mathrm{NW}}}{2\lambda_{\mathrm{sub},i}}} \Gamma_{\mathrm{sub},i} D_{\mathrm{sub},i}\lambda_{\mathrm{sub},i}\lambda_{\mathrm{NW},i} \\ +\sinh\left(\frac{L_{\mathrm{NW}}}{\lambda_{\mathrm{NW},i}}\right) K_{0,\frac{d_{\mathrm{NW}}}{2\lambda_{\mathrm{sub},i}}} \Gamma_{\mathrm{sub},i} D_{\mathrm{NW},i}\lambda^2_{\mathrm{sub},i} \\ +\left((\Gamma_{\mathrm{NW},i}\lambda^2_{\mathrm{NW},i} - \Gamma_{\mathrm{sub},i} D_{\mathrm{NW},i}\lambda^2_{\mathrm{sub},i}) \right. \\ \left. \times \cosh\left(\frac{L_{\mathrm{NW}}}{\lambda_{\mathrm{NW},i}}\right) + \Delta\Gamma_{\mathrm{al},i}\lambda_{\mathrm{NW},i} D_{\mathrm{sub},i}\right) K_{0,\frac{r}{\lambda_{\mathrm{sub},i}}} \end{pmatrix} \right] \times \left[\begin{matrix} \cosh\left(\frac{L_{\mathrm{NW}}}{\lambda_{\mathrm{NW},i}}\right) K_{1,\frac{d_{\mathrm{NW}}}{2\lambda_{\mathrm{sub},i}}} D_{\mathrm{sub},i}\lambda_{\mathrm{NW},i} \\ +\sinh\left(\frac{L_{\mathrm{NW}}}{\lambda_{\mathrm{NW},i}}\right) K_{0,\frac{d_{\mathrm{NW}}}{2\lambda_{\mathrm{sub},i}}} D_{\mathrm{NW},i}\lambda_{\mathrm{sub},i} \end{matrix} \right]^{-1}. \tag{39}$$

A.3. Temperature independent parameters used for GaAs NW growth modelling

Values without references are fitting parameters or estimated values.

Parameters	Values	Ref.
$\Xi'_{\mathrm{al,Ga}}$	$1\times10^{4}\,\mathrm{nm^{-1}\,s^{-1}}$	—
$\Xi'_{\mathrm{al,As}}$	$1\,\mathrm{nm^{-1}\,s^{-1}}$	—
$\Xi_{\mathrm{ls,III-V}}$	$1\times10^{3}\,\mathrm{nm^{-2}\,s^{-1}}$	at
$\times\exp\left(-\frac{\delta g^{\mathrm{TS,ERS}}_{\mathrm{ls,III-V}}}{k_{\mathrm{B}}T}\right)$		$T=630\,^{\circ}\mathrm{C}$
$\bar{Z}'_{\mathrm{aa,III}}, \bar{Z}'_{\mathrm{aa,V}}$	1×10^{-3}	—
$\bar{Z}'_{\mathrm{as,III}}\bar{Z}'_{\mathrm{as,V}}$	1×10^{-15}	—
$\bar{Z}'_{\mathrm{av,III}}, \bar{Z}'_{\mathrm{av,V}}$	1×10^{-2}	—
$\bar{Z}'_{\mathrm{av,III,sub}}, \bar{Z}'_{\mathrm{av,V,sub}}$	1×10^{-3}	—
$\Delta h^{\mathrm{ERS}}_{\mathrm{aa},\{1\,\bar{1}\,0\},\mathrm{Ga}}$	0.3 eV	[84]
$\Delta h^{\mathrm{ERS}}_{\mathrm{aa},\{1\,\bar{1}\,0\},\mathrm{As}}$	0.65 eV	[84]
$\Delta h^{\mathrm{ERS}}_{\mathrm{aa},\{1\,1\,1\},\mathrm{Ga}}$	0.3 eV	[84]
$\Delta h^{\mathrm{ERS}}_{\mathrm{av},\{1\,\bar{1}\,0\},\mathrm{Ga}}$	2.3 eV	[84]
$\Delta h^{\mathrm{ERS}}_{\mathrm{av},\{1\,\bar{1}\,0\},\mathrm{As_2}}$	2 eV	[84]
$\Delta h^{\mathrm{ERS}}_{\mathrm{av,SiO}_x,\mathrm{As}}//\Delta h^{\mathrm{ERS}}_{\mathrm{av,SiO}_x,\mathrm{Ga}}$	1 eV//1.5 eV	—
$\Delta h^{\mathrm{ERS}}_{\mathrm{as,SiO}_x,i}$	0 eV	—
$\gamma_{\mathrm{vs,ZB}\{1\,\bar{1}\,0\}}$	$4.98\,\mathrm{eV\,nm^{-2}}$	[85]
$\gamma_{\mathrm{vs,WZ}\{\bar{1}\,2\,\bar{1}\,0\}}$	$4.42\,\mathrm{eV\,nm^{-2}}$	[85]
$\gamma_{\mathrm{vs,ZB}\{3\,1\,1\}}/\gamma_{\mathrm{vs,WZ}\{\bar{1}\,2\,\bar{1}\,2\}}$	$7\,\mathrm{eV\,nm^{-2}}$	—
$\gamma_{\mathrm{vs,ZB}\{2\,0\,1\}}//\gamma_{\mathrm{vs,WZ}\{\bar{1}\,2\,\bar{1}\,1\}}$	$6\,\mathrm{eV\,nm^{-2}}$	—
$\gamma_{\mathrm{vs,ZB}\{3\,1\,2\}}/\gamma_{\mathrm{vs,WZ}\{\bar{1}\,2\,\bar{1}\,3\}}$	$7\,\mathrm{eV\,nm^{-2}}$	—
$\gamma_{\mathrm{vs,ZB}\{111B\}}/\gamma_{\mathrm{vs,WZ}\{1000B\}}$	$5\,\mathrm{eV\,nm^{-2}}$	—
γ_{vl}(liquid Ga)	$4.2\,\mathrm{eV\,nm^{-2}}$	[77]

A.4. Trigonometric relations for the single slice modelling

Following the single slice construction shown in figure 1(*b*), the associated trigonometric quantities are given by:

$$\vartheta(\Delta z_+, \Delta z_-, d_{\mathrm{NW}}) = \arctan\left(\frac{\Delta z_+ - \Delta z_-}{d_{\mathrm{NW}}}\right),$$

$$d_{\mathrm{eff}}(\Delta z_+, \Delta z_-, d_{\mathrm{NW}}) = \frac{d_{\mathrm{NW}}}{\cos(\vartheta)},$$

$$d_{\mathrm{top}}(\Delta z_+, \Delta z_-, \theta^+_{\mathrm{T}}, \theta^-_{\mathrm{T}}, d_{\mathrm{NW}}) = d_{\mathrm{NW}} - \Delta z_- \tan(\theta_{\mathrm{T}-}) - \Delta z_+ \tan(\theta_{\mathrm{T}+}),$$

$$R_{\mathrm{l}}(\Delta z_+, \Delta z_-, \mathrm{d_{NW}}, \xi) = \frac{d_{\mathrm{NW}}}{2\cos(\vartheta)\sin(\xi)},$$

$$H'_{\mathrm{l}}(\Delta z_+, \Delta z_-, d_{\mathrm{NW}}, \xi) = R_{\mathrm{l}} + \Xi(\xi)\sqrt{R_{\mathrm{l}}^2 - \left(\frac{d_{\mathrm{eff}}}{2}\right)^2},$$

$$\Xi(\xi) = \begin{matrix} 1 & \text{for} & \xi > \pi/2, \\ -1 & \text{for} & \xi < \pi/2. \end{matrix}$$

The volumes of the slice shown in figure 1(*c*) are given by

$$\Delta V_{\mathrm{s,low}\pm}(\Delta z_\pm, d_{\mathrm{NW}}) = \frac{d^2_{\mathrm{NW}}\mathrm{d}\omega^2}{8}(\Delta z_{\mathrm{ref}} - \Delta z_\pm),$$

$$\Delta V_{\mathrm{s,top}\pm}(\Delta z_\pm, \theta_{\mathrm{T}\pm}, d_{\mathrm{NW}}) = \frac{\mathrm{d}\omega}{6}\Delta z_\pm\left[3\left(\frac{d_{\mathrm{NW}}}{2}\right)^2 + (\Delta z_\pm\tan(\theta_{\mathrm{T}\pm}))^2 - \frac{3}{2}d_{\mathrm{NW}}\Delta z_\pm\tan(\theta_{\mathrm{T}\pm})\right],$$

$$\Delta V_{\mathrm{s,T}\pm}(\Delta z_\pm, \theta_{\mathrm{T}\pm}, d_{\mathrm{NW}}) = \frac{1}{12}\,\mathrm{d}\omega(\Delta z_\pm)^2\tan(\theta_{\mathrm{T}\pm}) \times (3d_{\mathrm{NW}} - 2\Delta z_\pm\tan(\theta_{\mathrm{T}\pm})),$$

and the total liquid and solid volumes are therefore given by

$$\Delta V_{\mathrm{l}}(\Delta z_+, \Delta z_-, \theta_{\mathrm{T}+}, \theta_{\mathrm{T}-}, d_{\mathrm{NW}}, \xi) = \frac{2d\omega}{2\pi} \times \frac{1}{3}\pi H_{\mathrm{l}}'^2(3R_{\mathrm{l}} - H'_{\mathrm{l}}) - (\Delta V_{\mathrm{s,top}-} + \Delta V_{\mathrm{s,top}+}),$$

$$\Delta V_{\mathrm{S}}(\Delta z_+, \Delta z_-, \theta_{\mathrm{T}+}, \theta_{\mathrm{T}-}, d_{\mathrm{NW}}) = \Delta V_{\mathrm{s,low}-} + \Delta V_{\mathrm{s,top}-} + \Delta V_{\mathrm{s,low}+} + \Delta V_{\mathrm{s,top}+},$$

respectively. The corresponding number of atoms in the respective phases are given by, $\Delta N_{\mathrm{l(s)}} = \Delta V_{\mathrm{l(s)}}/\Omega_{\mathrm{l(s)}}$, with $\Omega_{\mathrm{l(s)}}$ being the atomic volumes. The areas of the side-, truncation-, and top-facet (see figure 2(*a*)) are given by

$$\Delta A_{\mathrm{vl}}(\Delta z_+, \Delta z_-, d_{\mathrm{NW}}, \xi) = \frac{2d\omega}{2\pi}2\pi R_{\mathrm{l}}H'_{\mathrm{l}},$$

$$\Delta A_{\mathrm{ls}1\,1\,1}(\Delta z_+, \Delta z_-, \theta_{\mathrm{T}+}, \theta_{\mathrm{T}-}, d_{\mathrm{NW}}) = \frac{1}{2}d\omega[(d_{\mathrm{NW}} - \Delta z_+\tan(\theta_{\mathrm{T}+}))^2 + (d_{\mathrm{NW}} - \Delta z_-\tan(\theta_{\mathrm{T}-}))^2],$$

$$\Delta A_{\mathrm{ls\_T}\pm}(\Delta z_\pm, \theta_{\mathrm{T}\pm}, d_{\mathrm{NW}}) = \frac{1}{2}d\omega\frac{\Delta z_\pm}{\cos(\theta_{\mathrm{T}\pm})}(d_{\mathrm{NW}} - \tan(\theta_{\mathrm{T}\pm})\Delta z_\pm),$$

$$\Delta A_{\mathrm{vs}}(\Delta z_+, \Delta z_-, d_{\mathrm{NW}}) = (2\Delta z_{\mathrm{ref}} - \Delta z_- - \Delta z_+)\frac{d_{\mathrm{NW}}}{2}\,\mathrm{d}\omega.$$

A.5. Simulations of the truncation dynamics

Parameters for the simulations of the truncation dynamics are shown in table 4.

A.6. Including the effect of A triple line tension

An additional contribution to the free energy of the system may come from an in-balance of capillary forces meeting at the TL [45]. A change in one of the involved interface orientations implies a change in such a TL energy, and in order to reach mechanical equilibrium, an increase in strain per unit TL length in the solid and/or by a local change in the vl curvature on the cost of more vl interface is induced. Both effects alter the chemical potentials and can therefore have an influence on the growth dynamics. The effect of TL forces on the growth dynamics of NWs was introduced by Schwarz and Tersoff [45], who used the tangential component of the TL force on a locally smooth solid surface to describe the TL motion, and the normal component altering the solid chemical potential at the TL. We will here take a slightly different approach and

Table 1. Facets for ZB and WZ structure for the upper hemisphere with the lowest predicted surface energies are described with a set of angles (ω, θ) as shown in figure 6. Here $90^\circ - \theta = \theta_T = 90^\circ$ is defined to be the growth axis. See figure 19 for examples of truncation facets of the WZ crystal.

ZB facet normals			WZ facet normals	
$\omega = \{-30^\circ, 90^\circ \ldots\}$	$\omega = \{0^\circ, 60^\circ \ldots\}$	$\omega = \{30^\circ, 150^\circ \ldots\}$	$\omega = \{-30^\circ, 30^\circ \ldots\}$	$\omega = \{0^\circ, 60^\circ \ldots\}$
$\{2\,\bar{1}\,\bar{1}\}A$	$\{1\,0\,\bar{1}\}$	$\{1\,1\,\bar{2}\}B$	$\{0\,\bar{1}\,1\,0\}$	$\{\bar{1}\,2\,\bar{1}\,0\}$
$\theta_T = 0^\circ$	$\theta_T = 0^\circ$	$\theta_T = 0^\circ$	$\theta_T = 0^\circ$	$\theta_T = 0^\circ$
$\{3\,\bar{1}\,\bar{1}\}$	$\{3\,1\,\bar{1}\}$	$\{1\,1\,\bar{1}\}$	$\{0\,\bar{2}\,2\,1\}$	$\{\bar{1}\,2\,\bar{1}\,1\}$
$\theta_T = 10^\circ$	$\theta_T = 31.5^\circ$	$\theta_T = 19.5^\circ$	$\theta_T = 15.0^\circ$	$\theta_T = 17.1^\circ$
$\{1\,0\,0\}$	$\{2\,1\,0\}$	$\{2\,2\,\bar{1}\}$	$\{0\,\bar{1}\,1\,1\}$	$\{\bar{1}\,2\,\bar{1}\,2\}$
$\theta_T = 35.3^\circ$	$\theta_T = 50.8^\circ$	$\theta_T = 35.3^\circ$	$\theta_T = 28.1^\circ$	$\theta_T = 31.7^\circ$
$\{2\,1\,1\}$	$\{3\,2\,1\}$	$\{1\,1\,0\}$	$\{0\,\bar{1}\,1\,2\}$	$\{\bar{1}\,2\,\bar{1}\,3\}$
$\theta_T = 70.5^\circ$	$\theta_T = 67.8^\circ$	$\theta_T = 54.7^\circ$	$\theta_T = 46.9^\circ$	$\theta_T = 42.8^\circ$

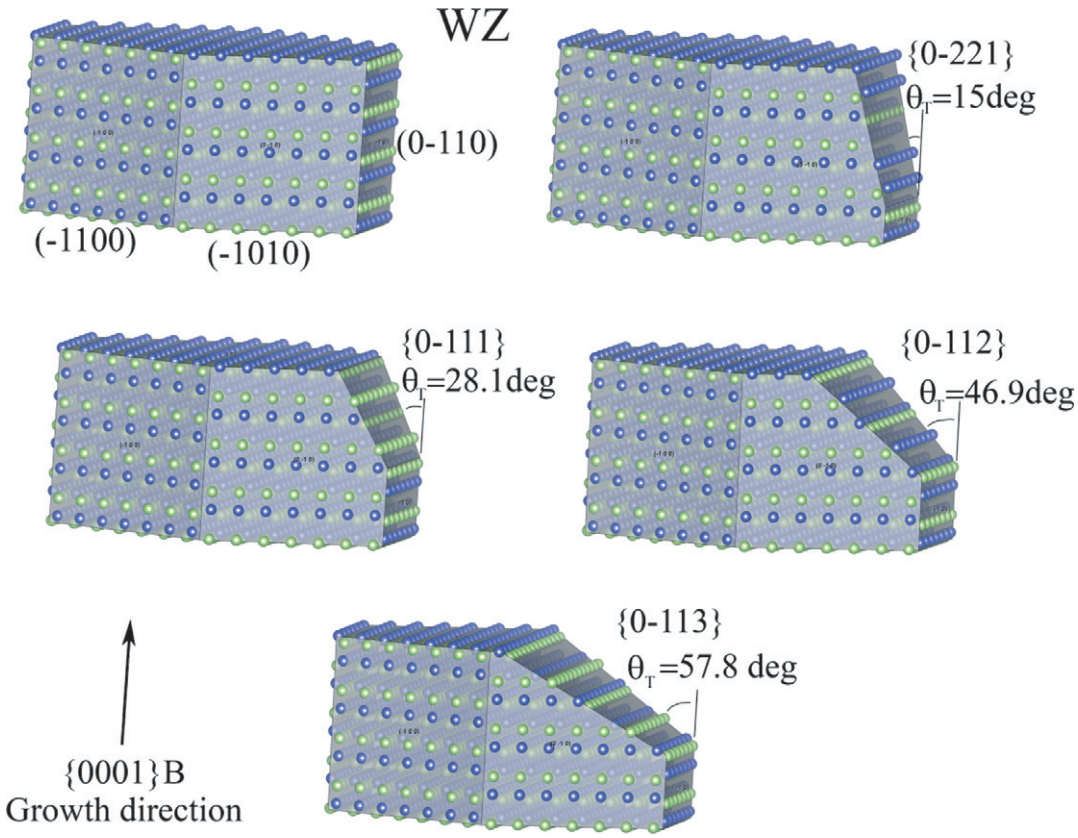

Figure 19. Axial segments of III–V WZ NWs with overall $\{1\,\bar{1}\,0\,0\}$ sidefaceting.

Table 2. The coefficients of the free energy expressions of the pure elements in the case of InAs and GaAs are taken from the SGTE database [86], and are relative to the to the enthalpy of the standard element reference (HSER). The interaction parameters are taken from Ansara *et al* [75]. T is the corresponding Kelvin temperature and all values are in Joule per mole. The equilibrium As mole fraction $x_{V,eq}$ is found from fitting liquidus values from [87], in the range $T = 400$–$800\,^\circ$C for ZB GaAs and $T = 350$–$550\,^\circ$C for ZB InAs. All equilibrium data are found from experimental measurements and are relying on thermodynamical parameters which therefore should coexist in kinetic equilibrium.

Liquid	$g_{Ga_{1-x}V As_xV}$ (J mole^{-1})	$g_{In_{1-x}V As_xV}$ (J mole^{-1})
$g'_{l,III}(T)$	$-1389.2 + 114.049T - 26.069\,299T\ln(T)$ $+1.0506 \times 10^{-4}T^2 - 4.0173 \times 10^{-8}T^3 - 118\,332T^{-1}$	$-3479.81 + 116.8358T - 27.4562T\ln(T)$ $+5.4607 \times 10^{-4}T^2 - 8.367 \times 10^{-8}T^3 - 211\,708T^{-1}$
$g'_{l,V}(T)$	$1.717\,245 \times 10^4 + 99.786\,39T - 23.3144T\ln(T)$ $-0.002\,716\,13T^2 + 11\,600T^{-1}$	$1.717\,245 \times 10^4 + 99.786\,39T - 23.3144T\ln(T)$ $-0.002\,716\,13T^2 + 11\,600T^{-1}$
$L_0(T)$	$-25\,503.6 - 4.3109 \cdot T$	$-15\,851 - 11.270\,53 \cdot T$
$L_1(T)$	-5174.7	-1219.5
$x_V^{ERS}(T)$	$6.752 \times 10^{-7}\exp(0.0141 \cdot T)/100$	$(9.9 \times 10^{-4}\exp(0.009\,72 \cdot T) - 0.3)/100$

Table 3. Thermodynamic data taking from Ansara *et al* [75], where $g_{\mathrm{v},i_n}^{\mathrm{pure}'n}(T) = \Psi_i'^n(T) + RT\ln(P)$, with P being the total vapour pressure in units of 0.1 MPa. T is the corresponding Kelvin temperature and all values are in Joule per mole.

Gas	$\Psi_i'^n(T)(\mathrm{J\,mole^{-1}})$
Ga	$263\,612.519 + 33.487\,1429T - 30.750\,07T\ln(T) + 0.005\,377\,45T^2 - 5.465\,34\times10^{-7}T^3 - 150\,942.65T^{-1}$
In	$237\,868.024 - 110.524\,313T - 8.405\,227T\ln T - 0.015\,6847T^2 + 2.211\,96333\times10^{-6}T^3 - 110\,674.05T^{-1}$
As	$272\,027.85 - 32.253\,3338T - 21.215\,51T\ln T + 4.389\,1495\times10^{-4}T^2 - 7.393\,995\times10^{-8}T^3 + 9666.555T^{-1}$
As_2	$179\,351.548 + 10.551\,9715T - 37.359\,66T\ln T - 5.618\,06\times10^{-5}T^2 - 2.130\,98\times10^{-8}T^3 + 104\,881.15T^{-1}$
As_4	$129\,731.745 + 230.754\,352T - 83.044\,65T\ln T - 2.514\,8475\times10^{-5}T^2 + 1.044\,4733\times10^{-9}T^3 + 252\,728.45T^{-1}$

Table 4. Six types of simulations of 15 s of Ga-catalysed GaAs growth in the single slice construction (see figures 18, 20 and 21). Initial conditions marked with a subscript $_0$. 15 s of growth was in all these cases enough to go into a quasi-steady-state growth mode. Basic growth conditions are in all cases: $f_{\mathrm{V}}/f_{\mathrm{III}} = 10$, $\mathrm{GR_{planar}} = 0.3\,\mu\mathrm{m\,h^{-1}}$ and $T = 630\,^{\circ}\mathrm{C}$. The time steps are $\Delta t = 0.001$ s and at $t = 0$ the liquid composition is $x_{\mathrm{As}} = 0.01$ and the truncation height is $\Delta z_{-,0} = \Delta z_{+,0} = -1$ nm. All simulations are modelling the formation of ZB structure at $\omega = 0^{\circ}$ where the structure is symmetric around the growth axis in the single slice construction. Parameters not given here are given in section A.3 in the appendix.

Simulation no.	$\theta_{\mathrm{T}-,0} = \theta_{\mathrm{T}+,0}$	ξ_0	w_{hkl}	σ	$\gamma_{\mathrm{vs}0}$	c_{hkl}
S1	50.8°	120°	10°	0.35	$10\,\mathrm{eV\,nm^{-2}}$	1
S2	50.8°	110°	8°	0.4	$9\,\mathrm{eV\,nm^{-2}}$	1
S3	50.8°	120°	15°	0.4	$9\,\mathrm{eV\,nm^{-2}}$	0.71
S4	31.5°	—	3°	0.4	$8\,\mathrm{eV\,nm^{-2}}$	1
S5	50.8°	—	15°	0.4	$9\,\mathrm{eV\,nm^{-2}}$	0.71
S6	50.8°	130°	15°	0.5	$9\,\mathrm{eV\,nm^{-2}}$	0.71

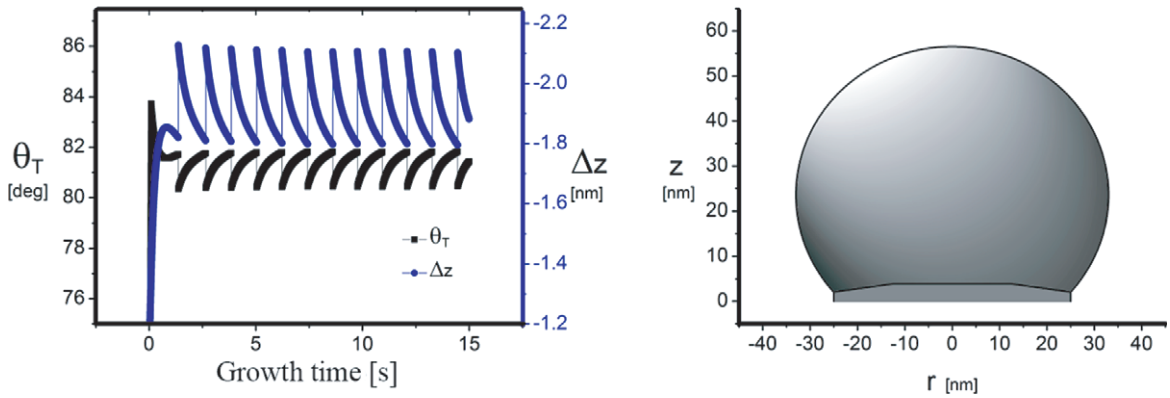

Figure 20. 15 s growth simulation (using simulation parameters S6 in table 4) of self-catalysed GaAs NW growth in the single slice construction. On the left, the truncation height and truncation angle are oscillating in coherent manner with periods of the formation of a ML at the topfacet. In this simulation the oscillations only fill up approximately a single ML at the truncation facets between each nucleation event at the topfacet. This means that the oscillations would be difficult to detect even in in-situ TEM experiments, however in this single slice construction it should be seen as kind of an average of the whole growth region. For the real 3D system, the oscillations seem to dominate on certain facets [40–42], which maybe an indication that edge energies may play an important role. The NW morphology after 15 s of growth is shown on the right.

let the TL equilibration allow take part in the total free energy minimization process in all dimensions. Because changes in the liquid volume induce changes in the TL excess, we assign the TL excess to the liquid phase for convenience and add an extra term to the liquid chemical potential as

$$\delta\mu_{\mathrm{l},i}(x_{\mathrm{III}}, x_{\mathrm{V}}, T, \omega) = \mu_{\mathrm{l},i}^{\infty}(x_{\mathrm{III}}, x_{\mathrm{V}}, T) + \gamma_{\mathrm{vl}}\frac{\partial A_{\mathrm{vl}}}{\partial N_{\mathrm{l},i}} + \frac{\mathrm{d}\Upsilon(\omega)}{\mathrm{d}N_{\mathrm{l},i}} - \mu_i^{\mathrm{ERS}}.$$

Here $\mathrm{d}\Upsilon(\omega)$ is the TL excess free energy per length at ω and Υ is the total TL excess. The effect of the TL force on crystal growth is difficult to quantify mainly because it has been difficult to measure experimentally. Nevertheless if we as in [45] define an effective width of the TL, w_{eff}, the TL force along the pq interfacial component can be written as,

$$f_{pq} = w_{\mathrm{eff}}(\gamma_{pq} + \gamma_{qw}\cos(\theta_q) + \gamma_{pw}\cos(\theta_p) + \tau\kappa_{pq}),$$

where pqw is any cyclic permutation of vls. τ is the line excess free energy depending on f_{pq} itself and κ_{pq} the line curvature at ω projected on the pq component (see figure 22 for a cross sectional illustration of the TL). Assuming the TL curvature is negligible, the net force along all interfaces at the TL in

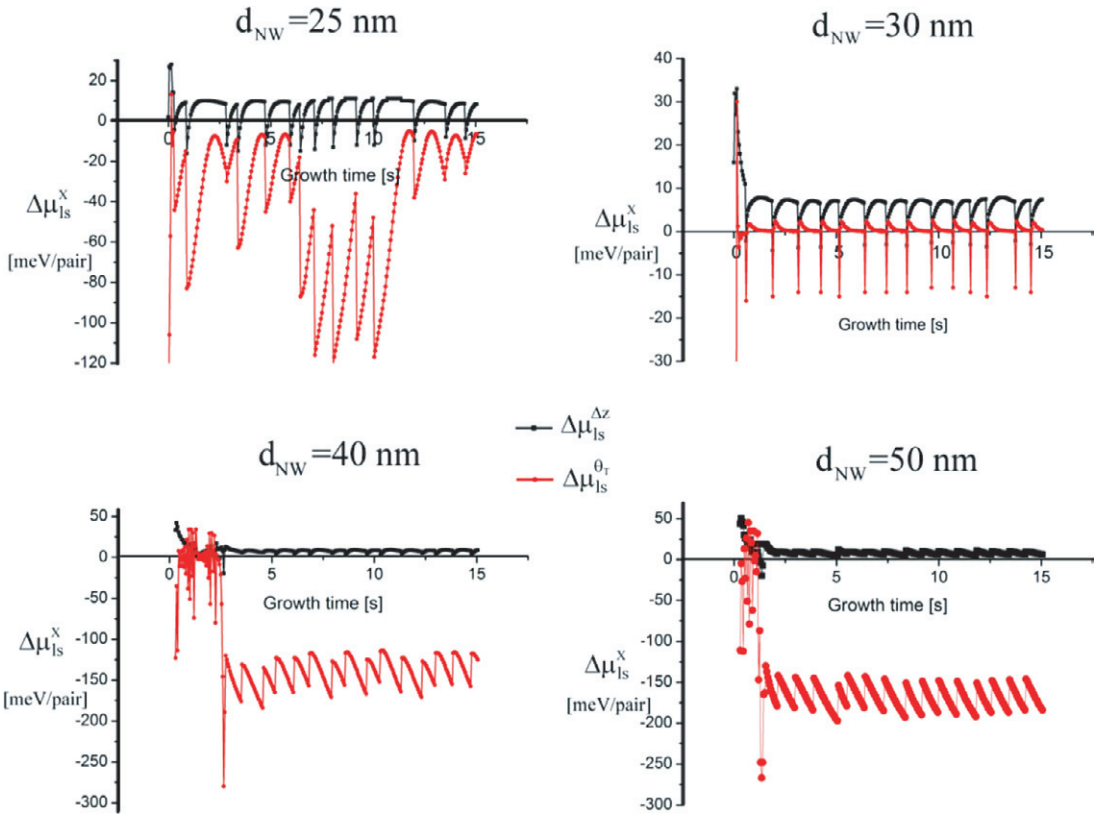

Figure 21. For a given set of initial conditions the ls driving forces forming the truncation facets are plotted as a function of 15 s of growth time (Growth simulations S1). At smaller diameters the growth system seems highly unstable which is due to not only the initial conditions but also to the solid anisotropy. For $d_{\mathrm{NW}} = 30$ nm the system moves into a steady-state regime not far from equilibrium, this means that the initial conditions are fitting well with the energies chosen for the system. At larger diameters the truncation facets moves into a steady-state regime far from local equilibrium.

equation (39) vanish at equilibrium, and the surface energies and corresponding contact angles are given by

$$\gamma_{pq} = \frac{\sin(\theta_{w,eq})}{\sin(\theta_{p,eq})}\gamma_{qw} \text{ and } \cos(\theta_{p,eq}) = \frac{\gamma_{qw}^2 - \gamma_{pq}^2 - \gamma_{pw}^2}{2\gamma_{pq}\gamma_{pw}}.$$

Away from equilibrium, we will describe the TL excess per length as,

$$\mathrm{d}\Upsilon(\omega) = \frac{d_{\mathrm{NW}}(\omega)}{2}\,\mathrm{d}\omega|f_{\mathrm{TL}}(\theta_{\mathrm{l}}(\omega), \theta_{\mathrm{s}}(\omega))|$$

with $|f_{\mathrm{TL}}(\theta_{\mathrm{l}}, \theta_{\mathrm{s}})| = \sqrt{f_{\mathrm{ls}||}^2 + f_{\mathrm{ls}\perp}^2 + \tau^2\kappa^2} = w_{\mathrm{eff}}[(\gamma_{\mathrm{ls}} + \gamma_{\mathrm{vs}}\cos(\theta_{\mathrm{s}}) + \gamma_{\mathrm{vl}}\cos(\theta_{\mathrm{l}}))^2 + (\gamma_{\mathrm{vs}}\sin(\theta_{\mathrm{s}}) - \gamma_{\mathrm{lv}}\sin(\theta_{\mathrm{l}}))^2 + \tau^2\kappa^2]^{1/2}$ being the net force per length at ω. To see the effect induced by the TL tension around the TL, evolution of the local morphology may be described by a local curvature dependent driving force as in [45].

A.7. Geometrical analysis of a constant vl curvature construction and total facetting, $\eta(\omega) = 0$

To analyse the total liquid–solid dynamics we need to include the ω-dependence on all parameters in the parameter set, $\{X(\omega)\}$. However this is as mentioned a very complex problem and we will here only make some rough simplifications in order to get qualitative ideas and better understanding about

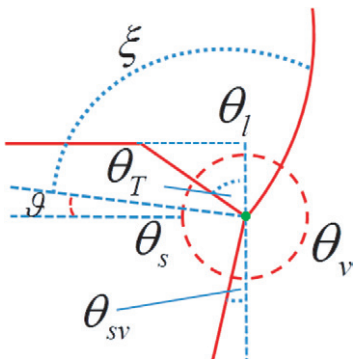

Figure 22. Cross sectional view on the TL (green dot). The red solid lines illustrate the actual morphology at the TL region at the given ω, and the blue dotted lines illustrates the construction lines.

the three-dimensional system. As compared to the single slice construction above at least one additional parameter, namely $\eta(\omega)$ (see equation (18)), needs to be added to the parameter set. If the liquid is assumed to have a constant curvature an example of a choice of parameter set could be; $\{X(\omega)\} \in \{d_{\mathrm{NW}}, \eta, \Delta z_+, \Delta z_-, \theta_{\mathrm{T}+}, \theta_{\mathrm{T}-}, \xi\}$. The form of $\eta(\omega)$ which describes the cross sectional shape of the growth interface, is very important for the total configuration but it is also a very complex parameter to include. It has not been possible in the time of writing to find a consistent method

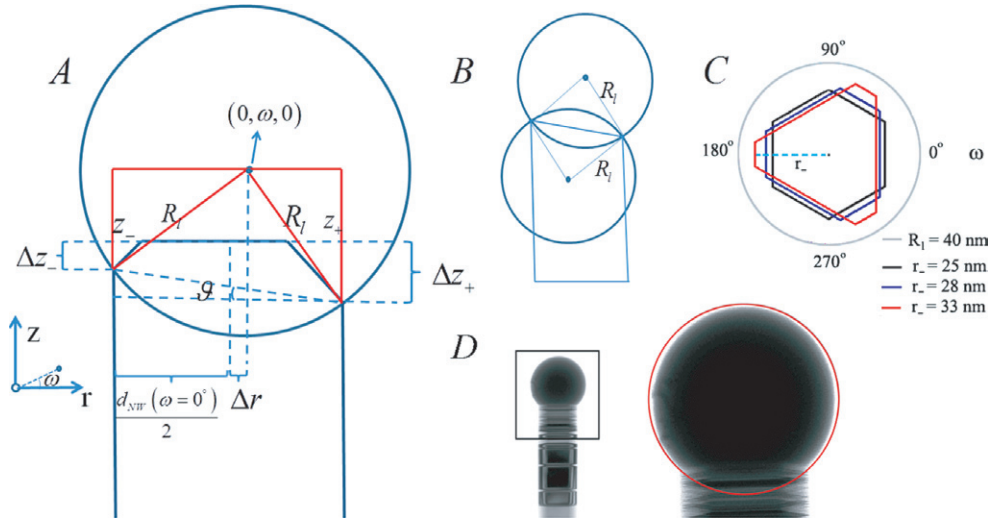

Figure 23. (*a*) Illustration of the trigonometry used to derive the Δz versus ω relation for the constant vapour–liquid curvature construction and $\eta(\omega) = 0$. (*b*) For a given radius of curvature there exist two solutions, one for $\xi \geqslant 90^\circ$ and one for $\xi < 90^\circ$. (*c*) If we allow for a three-fold symmetric morphology we need to define two lengths, r_- and r_+, to describe the diameter. However for a given crystal volume only r_- is needed, see equation (19). (*d*) A TEM image along the [1 $\bar{1}$ 0] zone axis of a GaAs NW with a Ga droplet on top. The red circle on the enlarged view is a perfect circle, which fits almost perfect to the shape of the Ga droplet.

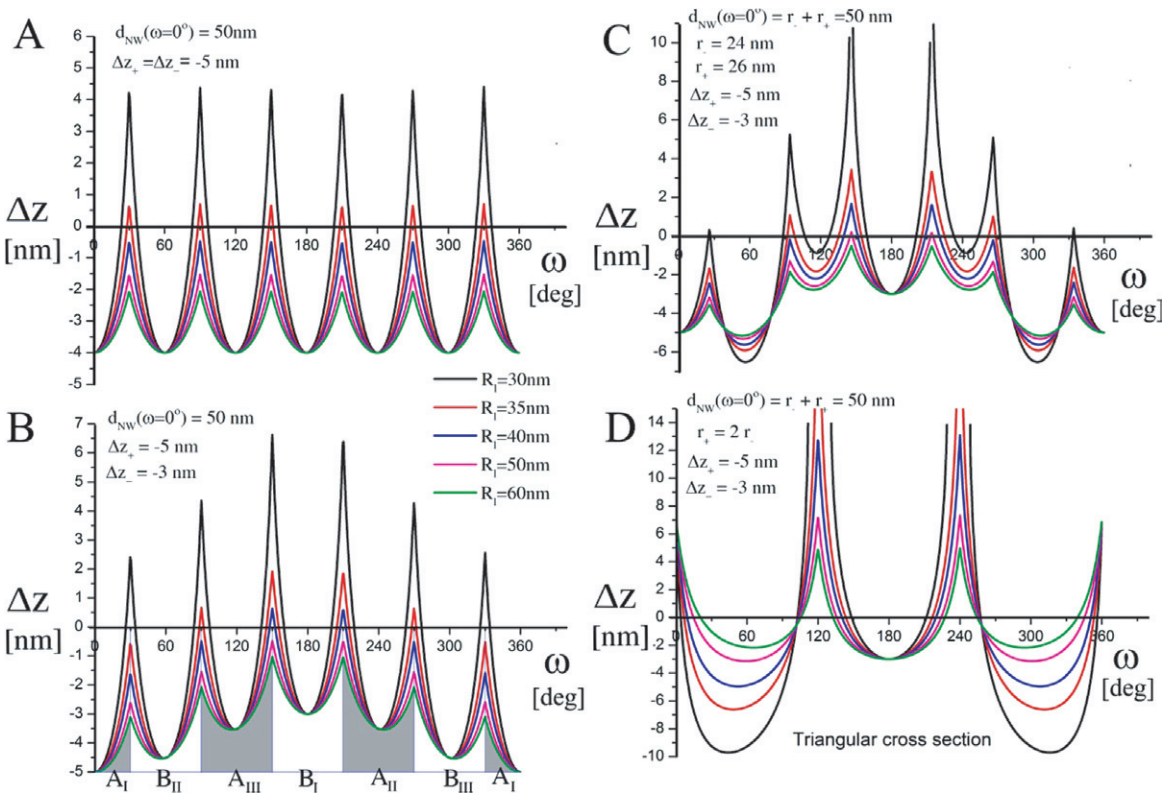

Figure 24. Geometrical representation of the truncation size, Δz, as a function of ω and different liquid sizes, for a NW system with $d_{\mathrm{NW}}(\omega = 0^\circ) = 50$ nm assuming constant vapour–liquid curvature and total facetting at the same time. (*a*) Assuming equal truncation $\Delta z_- = \Delta z_+$at both sides at $\omega = 0^\circ$, as initial conditions on a complete facetted solid hexagonal cross section. (*b*) If the crystal has three-fold symmetry but takes on a six-fold morphology it can be favourable to incline the growth system. However, assuming vertical sidewalls it can be shown that the system does not lower the free energy because the areas of A and B type facets are the same in total (indicated by grey and white regions) and the system either chooses to make the A facets smaller and the B facets larger as shown in (*c*). It should be noted that an inclination angle could be initiated by a non-isotropic incoming vapour flux due to the Marangoni effect [88] but this is out of the scope of this study. In (*c*) it is seen that if the solid induce even a small derivation from the hexagonal shape, it has a huge impact on the growth system which will most likely also be present in the real system. (*d*) In the extreme case of a triangular shaped NW and constant vl curvature, the system will be in regime I for all truncation sizes in the case of $R_l > 37$ nm around the edges of the triangle. This is because there is no solution to the sidefacet-liquid intersection problem. In this case the edges will be either rounded or TL has moved in on the topfacet and the facet edges may be completed by surface diffusion.

to solve this system. In this section we will instead show some implications of typical assumptions used for modelling NW growth, which will serve as instructive and informative insight to the three-dimensional anisotropic ls system. Such as under which configurations and conditions the NW growth system will move in and out of regimes I and II. The free energy minimization process of the ls system during growth is complex mainly due to the interplay between the isotropic liquid and the anisotropic solid. If we imagine that the cusps of the gamma plot shown in figures 6(*b*) or (*c*) are very sharp and deep, then the system will choose total sidewall facetting even at the TL, and the liquid phase will 'adjust' to this as long as the system is regime II. In an ideal regime I (a single planar ls topfacet) the nucleation statistics can be treated in the framework proposed in [26], which is mainly a relevant regime during changes in growth conditions where the relative size of the liquid is decreasing. If we furthermore assume that the vl interface tension is strong, the isotropic (and assumed homogeneous) liquid prefers a constant curvature due to a strong Laplace pressure. To describe such a system we will first choose a single slice construction which is oriented in such a way that $\omega = 0^\circ$ is in the direction of the liquid–solid displacement, Δr (see figure 23(*a*)). Using cylindrical coordinates, (r, ω, z), we can write two intersections between the wire and liquid as $(r_-, 180^\circ, z_-)$ and $(r_+, 0^\circ, z_+)$. For a given radius of curvature there exist two solutions, one for $\xi \geqslant 90^\circ$ and one for $\xi < 90^\circ$, as seen in figure 23(*b*). Here

$$z_- = -\frac{\Delta}{2} - \frac{d_{\mathrm{NW0}}}{2}\sqrt{\frac{4R_{\mathrm{l}}^2 - \Delta^2 - d_{\mathrm{NW0}}^2}{\Delta^2 + d_{\mathrm{NW0}}^2}},$$

and the two intersections are given by

$$\left.\begin{aligned}(r_-, 180^\circ, z_-) &= \left(-\sqrt{R_{\mathrm{l}}^2 - z_-^2}, 180^\circ, z_-\right)\\ (r_+, 0^\circ, z_+) &= \left(-\sqrt{R_{\mathrm{l}}^2 - z_+^2}, 0^\circ, \Delta + z_-\right)\end{aligned}\right\} \quad \text{for } \xi \geqslant 90,$$

$$\left.\begin{aligned}(r_-, 180^\circ, z_-)' &= (-r_+, 0^\circ, -z_+)\\ (r_+, 0^\circ, z_+)' &= (-r_-, 180^\circ, -z_-)\end{aligned}\right\} \quad \text{for } \xi \leqslant 90,$$

where $\Delta = \Delta z_- - \Delta z_+$ is difference in truncation in the two sides and d_{NW0} is the diameter at $\omega = 0^\circ$. The z-coordinate for intersection between wire and liquid as a function of ω are then given by, $z(\omega) = -\sqrt{R_{\mathrm{l}}^2 - (\cos(\omega)d_{\mathrm{NW}}(\omega) + \Delta r)^2 - (\sin(\omega)d_{\mathrm{NW}}(\omega))^2}$, where $\Delta r = \sin(\vartheta)\sqrt{R_{\mathrm{l}}^2 - (d_{\mathrm{NW0}}^2/4\cos(\vartheta)^2)}$ is the displacement between of centre of the NW crystal and the liquid centre at $\omega = 0^\circ$. Now analysing the wetting consequences when assuming total sidefacetting ($\eta(\omega) = 0$ in equation (18)) will give us some qualitative ideas about the real system and under which conditions TL nucleation can take place, as shown in C.

In figure 24 the truncation heights are plotted for different relative sizes of the droplets and for six-fold and three-fold facetting. It is obvious that a relative large droplet will have a smaller probability of inducing positive truncations and it is also obvious that a hexagonal shape is the most convenient shape in relation with a liquid. If we allow for a three-fold facetting we need to define two lengths, r_- and r_+, to describe the diameter, see figure 24(*c*). It is very likely that for real systems that the truncation is negative all the way around the TL and only becomes positive at a given location when the liquid supersaturation is high and induce either TL nucleation or move the TL into regime I. A TEM image along the [1 $\bar{1}$ 0] zone axis of a GaAs NW with a Ga droplet on top is shown in figure 21(*d*). The red circle on the enlarged view is a perfect circle, which fits almost perfect to the shape of the Ga droplet. Thus if the liquid curvature is constant also as a function of ω, we can say that if the NW crystal completely faceted ($\eta_0 = 0$), the truncation height would vary as a function of ω as shown in . In the other extreme if the system is completely axi-symmetric $\eta_0 = 1$ the truncation height would be independent of ω. It is important to note that for real liquid–solid growth systems using the η_0 parameter to describe the system would give a value somewhere in between 0 and 1, and the amplitude of the curves in figure 24 will be smaller. See the figure text for a discussion of different cases of total facetting and constant liquid curvature.

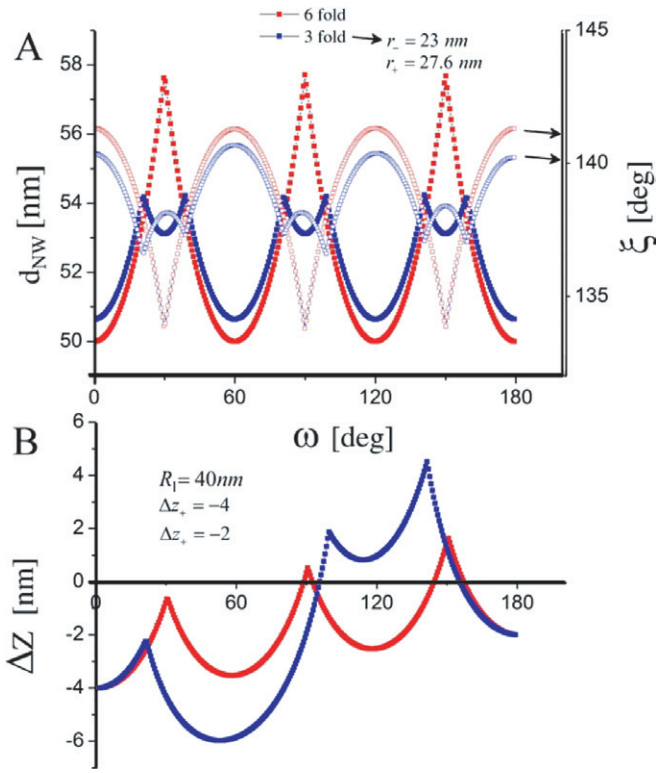

Figure 25. Comparison between a perfect six-fold hexagonal shaped NW (red) and a three-fold cross sectional morphology (blue) for a given crystal volume, under the assumption of constant vl curvature and total facetting. (*a*) The solid dots represent the NW diameter and the open dots represent the contact angle. (*b*) In the case of a strong driving force towards three-fold sidewall facetting it is likely that the TL will move in on the topfacet, here in the region around $\omega \sim 120^\circ$. For $\omega \in [180^\circ, 360^\circ]$, the curves are mirrored in $\omega = 180^\circ$.

In figure 25 we see the relationship between parameters; d_{NW}, ξ, Δz and ω under six-fold and three-fold symmetric sidewall facetting in the case of constant liquid curvature.

References

[1] Mourik V *et al* 2012 *Science* **336** 1003–7
[2] Lieber C M 2011 *MRS Bull.* 36
[3] Bulgarini G *et al* 2012 *Nature Photon.* **6** 455–8
[4] Kelzenberg M D *et al* 2010 *Nature Mater.* **9** 239–44
[5] Yan R, Gargas D and Yang P D 2009 *Nature Photon.* **3** 569–76
[6] Heiss M *et al* 2013 *Nature Mater.* **12** 439–44
[7] Krogstrup P *et al* 2013 *Nature Photon.* **7** 306–10
[8] Hu Y, Kuemmeth F, Lieber C M and Marcus C M 2012 *Nature Nanotechnol.* **7** 47
[9] Wagner R S and Ellis W S 1964 *Appl. Phys. Lett.* **4** 5
[10] Johansson J, Bolinsson J, Ek M, Caroff P and Dick K A 2012 *ACS Nano* **6** 7
[11] Krogstrup P, Yamasaki J, Sørensen C B, Johnson E, Wagner J B, Pennington R, Aagesen M, Tanaka N and Nygård J 2009 *Nano Lett.* **9** 3689
[12] Givargizov E I 1975 *J. Cryst. Crowth* **31** 20
[13] Hiruma K, Yazawa M, Katsuyama T, Ogawa K, Haraguchi K, Koguchi M and Kakibayashi H 1995 *J. Appl. Phys.* **77** 447
[14] Dubrovskii V G and Sibirev N V 2004 *Phys. Rev.* E **70** 031604
[15] Dubrovskii V G, Sibirev N V and Cirlin G E 2004 *Tech. Phys. Lett.* **30** 8
[16] Dubrovskii V G, Cirlin G E, Soshnikov I P, Tonkikh A A, Sibirev N V, Samsonenko Yu B and Ustinov V M 2005 *Phys. Rev.* B **71** 205325
[17] Johansson J, Svensson C P T, Mårtensson T, Samuelson L and Seifert W 2005 *J. Phys. Chem.* B **109** 13567–71
[18] Dick K A *et al* 2005 *Nano Lett.* **5** 761–4
[19] Dubrovskii V G; Sibirev N V, Harmand J C and Glas F 2008 *Phys. Rev.* B **78** 235301
[20] Johansson J, Karlsson L S, Svensson C P T, Mårtensson T, Wacaser B A, Deppert K, Samuelson L and Seifert W 2006 *Nature Mater.* **5** 574–80
[21] Madsen M H *et al* 2013 *J. Cryst. Growth* **364** 16
[22] Krogstrup P, Popovitz-Biro R, Johnson E, Madsen M H, Nygård J and Shtrikman H 2010 *Nano Lett.* **10** 4475
[23] Ramdani M R, Harmand J C, Glas F, Patriarche G and Travers L 2013 *Cryst. Growth Des.* **13** 91
[24] Li A, Sibirev N V, Ercolani D, Dubrovskii V G and Sorba L 2013 *Cryst. Growth Des.* **13** 2
[25] Glas F, Harmand J-C and Patriarche G 2007 *Phys. Rev. Lett.* **99** 146101
[26] Krogstrup P, Curiotto S, Johnson E, Aagesen M, Nygård J and Chatain D 2011 *Phys. Rev. Lett.* **106** 125505
[27] Yu X, Wang H, Lu J, Zhao J, Misuraca J, Xiong P and Molnaìr S V 2012 *Nano Lett.* **10** 12
[28] Wallentin J, Ek M, Wallenberg L R, Samuelson L, Deppert K and Borgström M T 2010 *Nano Lett.* **10** 12
[29] Hocevar M *et al* 2012 *Nature Commun.* **3** 737
[30] Caroff P, Dick K A, Johansson J, Messing M E, Deppert K and Samuelson L 2009 *Nature Nanotechnol.* **4** 50–5
[31] Gudiksen M S, Lauhon L J, Wang J, Smith D C and Lieber C M 2002 *Nature* **405** 617
[32] Dick K A, Caroff P, Bolinsson J, Messing M E, Johansson J, Deppert K, Wallenberg L R and Samuelson L 2010 *Semicond. Sci. Technol.* **25** 2
[33] Algra R E, Verheijen M A, Borgström M T, Feiner L-F, Immink G, van Enckevort W J P, Vlieg E and Bakkers E P A M 2008 *Nature* **456** 369–72
[34] Hofmann S *et al* 2008 *Nature Mater.* **7** 372–5
[35] Fontcuberta i Morral A, Colombo C, Abstreiter G, Arbiol J and Morante J R 2008 *Appl. Phys. Lett.* **92** 063112
[36] Haraguchi K, Katsuyama T, Hiruma K and Ogawa K 1992 *Appl. Phys. Lett.* **60** 745–7
[37] Yu X, Wang H, Lu J, Zhao J, Misuraca J, Xiong P and Molnaìr S V 2012 *Nano Lett.* **12** 10
[38] Munchi A M *et al* 2013 *J. Cryst. Growth* **372** 1
[39] Wen C-Y, Tersoff J, Reuter M C, Stach E A and Ross F M 2010 *Phys. Rev. Lett.* **105** 195502
[40] Oh S-H *et al* 2010 *Science* **330** 489
[41] Gamalski A D, Ducati C and Hoffmann S 2011 *J. Phys. Chem.* C **115** 4413
[42] Wen C-Y *et al* 2011 *Phys. Rev. Lett.* **107** 025503
[43] Krogstrup P, Madsen M, Hu W, Kozu M, Nakata Y, Nygård J, Takahasi M and Feidenhans'l R 2012 *Appl. Phys. Lett.* **100** 093103
[44] Harmand J-C, Glas F and Patriarche G 2010 *Phys. Rev.* B **81** 235436
[45] Schwarz K W and Tersoff J 2009 *Phys. Rev. Lett.* **102** 206101
[46] Schwarz K W and Tersoff J 2012 *Nano Lett.* **12** 1329–32
[47] Eisenhawer B, Sivakov V, Christiansen S and Falk F 2013 *Nano Lett.* **13** 3
[48] Eyring H 1935 *J. Chem. Phys.* **3** 107–15
[49] Glas F 2010 *J. Appl. Phys.* **108** 073506
[50] Hommeril F and Mutaftschiev B 1988 *Phys. Rev.* B **40** 296
[51] Carter W C, Roosen A R, Cahn J W and Taylor J E 1995 *Acta Metall. Mater.* **43** 4309
[52] Taylor J E 1992 *Acta Metall. Mater.* **40** 1475–85
[53] Schmidt V, Senz S and Gösele U 2005 *Appl. Phys.* A **80** 445–50
[54] Glas F 2010 *Phys. Status Solidi* b **247** 254–8
[55] Rieger T, Heiderich S, Lenk S, Lepsa M I and Grützmacher D 2012 *J. Cryst. Growth* **353** 1
[56] Tchernycheva M, Travers L, Patriarche G, Glas F, Harmand J-C, Cirlin G E and Dubrovskii V G 2007 *J. Appl. Phys.* **102** 094313
[57] Jong E D, LaPierre R R and Wen J Z 2010 *Nanotechnology* **21** 045602
[58] Connell J G *et al* 2013 *Nano Lett.* **13** 199
[59] Dick K A, Bolinsson J, Borg B M and Johansson J 2012 *Nano Lett.* **12** 6
[60] Cahn J W 1960 *Acta Metall.* **8** 554–62
[61] Yeh C-Y, Lu Z W, Froyen S and Zunger A 1992 *Phys. Rev.* B **45** 12130
[62] Yeh C-Y, Lu Z W, Froyen S and Zunger A 1992 *Phys. Rev.* B **46** 10086
[63] Glas F, Harmand J-C and Patriarche G 2010 *Phys. Rev. Lett.* **104** 135501
[64] Becker R and Döring W 1935 *Ann. Phys.* **24** 719
[65] Burton W K, Cabrera N and Frank F C 1951 *Phil. Trans. R. Soc. Lond.* A **243** 299–358
[66] Markov I 2003 *Crystal Growth for Beginners* 2nd edn (Singapore: World Scientific)
[67] Yeh C-Y, Lu Z W, Froyen L S and Zunger A 1992 *Phys. Rev. Lett.* **46** 10086
[68] Dubrovskii V G, Cirlin G E, Sibirev N V, Jabeen F, Harmand J C and Werner P 2011 *Nano Lett.* **11** 1247–53
[69] Schwalbach E J, Davis S H, Voorhees P W, Wheeler D and Warren J A 2011 *J. Mater. Res.* **26** 17
[70] Redlich O and Kister A 1948 *Ind. Eng. Chem.* **40** 345–8
[71] Ansara I *et al* 1994 *Calphad* **18** 2
[72] Russo-Averchi E, Heiss M, Michelet L, Krogstrup P, Nygard J, Magen C, Morante J R, Uccelli E, Arbiol J and Fontcuberta i Morral A 2012 *Nanoscale* **4** 5
[73] Uccelli E *et al* 2011 *Nano Lett.* **11** 9
[74] Ambrosini S, Fanetti M, Grillo V, Franciosi A and Rubini S 2011 *AIP Adv.* **1** 042142
[75] Colombo C, Spirkoska D, Frimmer M, Abstreiter G and Fontcuberta i Morral A 2008 *Phys. Rev.* B **77** 155326
[76] Dick K A, Caroff P, Bolinsson J, Messing M E, Johansson J, Deppert K, Wallenberg L R and Samuelson L 2010 *Semicond. Sci. Technol.* **25** 024009

[77] Cirlin G E *et al* 2010 *Phys. Rev.* B **82** 035302
[78] Jabeen F, Grillo V, Rubini R and Martelli F 2008 *Nanotechnology* **9** 275711
[79] Spirkoska D *et al* 2009 *Phys. Rev.* B **80** 245325
[80] Bauer B, Rudolph A, Soda M, A. Fontcuberta i Morral, Zweck J, Schuh D and Reiger E 2010 *Nanotechnology* **21** 43
[81] Plissard S, Larrieu G, Wallart X and Caroff P 2011 *Nanotechnology* **22** 27
[82] Wulff G 1901 *Z. Krystallogr. Mineralogie* **34** 449
[83] Dubrovskii V *et al* 2009 *Phys. Rev* B **79** 205316
[84] Activation enthalpies are based on DFT calculations are taken from the works; Pankoke V, Sakong S and Kratzer P 2012 *Phys. Rev.* B **86** 085425
Shapiro J N, Lin A and Huffaker D L 2011 *Phys. Rev.* B **84** 085322
[85] Pankoke V, Kratzer P and Sakong S 2011 *Phys. Rev.* B **84** 075455
[86] Dinsdale A T 1991 *Calphad* **15** 317–425
[87] Tmar M, Gabriel A, Chatillon C and Ansara I 1984 *J. Cryst. Growth* **69** 421–41
[88] Abbasoglu S and I Sezai 2007 *Eng. Comput.* **23** 2